



# Noise mitigation in rectangular jets through plasma actuator-based shear layer control

Anirudh Lakshmi Narasimha Prasad<sup>1,†</sup> and S. Unnikrishnan<sup>1</sup>

<sup>1</sup>Department of Mechanical Engineering, FAMU-FSU College of Engineering, Florida State University, Tallahassee, FL 32310, USA

(Received 21 June 2023; revised 19 September 2023; accepted 28 November 2023)

A computational analysis is performed to study the three-dimensional response of rectangular shear layers to plasma actuator-based control, in the context of sound mitigation of supersonic non-axisymmetric jets. A Mach 1.5 rectangular jet with an aspect ratio 2 : 1 is controlled using experimentally informed actuation patterns, referred to as M0, M1, M2, M3, M $\pi$  and M+/-1. While the first five progressively increase the phase difference between successive actuators thus enhancing three-dimensionality of the shear layer structures, the latter corresponds to the flapping mode of the jet. A preliminary linear analysis identifies that the frequency,  $St \sim 1$ , has a relatively high overall amplification within the baseline shear layer, and is hence utilized for control in the subsequent nonlinear simulations. Each actuation reveals unique near-field vortical and acoustic responses that have a profound impact on far-field noise levels. The M0 actuation induces circumferentially interconnected strong streamwise vortices, while M1 actuation enhances the circumferential variability in the coherent structures. The M2 actuation encompasses both these effects, and along with a very low tonal impact of forcing, produces the most desirable far-field noise mitigation ( $\sim 2.6$  dB), contributed by a broadband reduction around the column-mode peak of the baseline jet. Beyond M2 actuation, effectiveness of control saturates, particularly along the direction of peak noise radiation. Through a near-field analysis of the acoustic component, the efficacy of M2 actuation is attributed to the attenuation of the radiative efficiency of the jet, including reduced energy in the supersonic phase speeds, and redistribution of energy into the higher helical modes. Further, it curtails the nonlinear difference interactions in the plume that energize column-mode frequencies, which often appear as strong intermittent sound-producing events. While the shear layer turbulent kinetic energy decreases with actuation, the controlled jets show minimal variations in mean flow properties, particularly under M2 actuation, suggesting this to be a promising small-perturbation-based noise control strategy.

† Email address for correspondence: [al20di@fsu.edu](mailto:al20di@fsu.edu)

**Key words:** aeroacoustics, jet noise, noise control

---

## 1. Introduction

Controlling jet noise is critical to the safe, sustainable and efficient operation of military and civil aviation. In addition to the health hazards caused from exposure to intense noise levels of exhaust jets (Helfer 2011), high-amplitude acoustic emissions can induce damage to aircraft structure (Clarkson 1959), nearby establishments (Stephens & Mayes 1979) and the environment (Shannon *et al.* 2016). The present work pertains to the study of noise control strategies for supersonic rectangular nozzles typically utilized in military aircraft, that are often associated with high noise levels.

Key advantages associated with rectangular nozzles include improved air-frame integration features and reduced drag penalty (Wiegand 2018), as compared with an axisymmetric nozzle. However, the plumes of rectangular nozzles are relatively more complex in relation to well-characterized axisymmetric nozzles. This is attributed to additional flow mechanisms including the difference in core collapse rates between the two primary planes (major and minor axes) (Gutmark & Grinstein 1999), the associated asymmetry in hydrodynamic and acoustic signatures, axis switching (Valentich, Upadhyay & Kumar 2016), spatial non-homogeneity and dynamics of corner vortices (Zaman 1996), azimuthal vortex warping (Grinstein 1995) and preferential flapping about the minor axis plane (Gutmark, Schadow & Bicker 1990). The relative significance of the above mechanisms are also dependent on the aspect ratio (AR) of the nozzle and expansion conditions, resulting in a wide parameter space. These factors can strongly influence the noise sources and acoustic directivity of non-axisymmetric jets.

In the above context, to simplify the parameter space and focus on mitigating fundamental mechanisms responsible for peak noise radiation, we utilize an  $AR = 2 : 1$  perfectly expanded jet to present our noise control studies. Furthermore, this choice is also motivated by the availability of validation data in open literature. Far-field acoustics of such low AR jets has similarities with that of axisymmetric jets (Bridges 2012; Heeb *et al.* 2013). This includes prevalence and radiative effectiveness of lower azimuthal modes (Michalke & Fuchs 1975) and establishment of a near-axisymmetric (mean) plume, away from the nozzle exit. These similarities are useful while strategizing noise control techniques based on past experience on circular jets.

Both passive (Martens 2002; Liu *et al.* 2022) and active (Alvi *et al.* 2008; Prasad & Morris 2020) control techniques have been explored to reduce noise emissions from high-speed jets. In the current work we focus on an active control strategy based on localized arc filament plasma actuators (LAFPA) (Samimy *et al.* 2007a,b). If successful, active techniques are desirable for military aircraft due to their versatility to operate in a wide variety of temperature and expansion ratios. In addition, we rely on a small-perturbation-based control strategy, wherein the resulting basic state of the controlled jet is not significantly altered from that of the baseline jet. This potentially makes such control techniques scalable, without significant overhead.

For scalability, such small-perturbation-based techniques must be able to exploit the inherent instabilities of the shear layer. The nascent shear layer exiting the nozzle is sensitive to Kelvin–Helmholtz instability waves, with maximum amplification rates observed in the spectral vicinity of  $0.009 \leq St_\theta \leq 0.017$  (Michalke 1965; Gutmark & Ho 1983; Hussain 1986). Here  $St_\theta$  is the non-dimensional frequency, Strouhal number, based on the momentum thickness at the nozzle exit,  $\theta$ . Recent studies by Bogey (2022) have also

shown that for an axisymmetric nozzle with laminar exit conditions, the most amplified instability varies with Mach number between  $St_\theta = 0.018$  for  $M = 0.5$  to  $St_\theta = 0.0025$  for  $M = 2.0$ . The azimuthal mode of the instability was also observed to be sensitive to the jet Mach number. Upon exciting these instabilities, we expect their streamwise evolution to modify the coherent shear layer structures (in the baseline) in a manner conducive to reducing the acoustic gain of the jet, thus resulting in a quieter far field. A detailed discussion on the evolution of such excited shear layer instabilities can be found in the recent experimental work of Samimy *et al.* (2023), and references therein.

Based on experimental evidence from axisymmetric jets (Samimy, Kim & Kearney-Fischer 2009; Samimy *et al.* 2010), the most prominent parameters that determine the control authority of LAFPA actuators are the frequency and azimuthal mode of excitation. This is supported by corresponding simulations (Gaitonde & Samimy 2010, 2011) that have characterized spatio-temporal evolution of the axisymmetric and higher helical coherent shear layer structures generated in circular supersonic jets, through LAFPA-based actuation. For example, forcing the jet at its column-mode frequency (Petersen & Samet 1988),  $St \sim 0.3$ , results in large toroidal vortices as seen in computations by Gaitonde (2012), which amplifies downstream acoustic radiation. Here  $St$  is the Strouhal number, based on the nozzle diameter (or equivalent diameter). The above experiments (Samimy *et al.* 2009, 2010) also demonstrate that LAFPA can be used as a noise control strategy, capable of broadband reduction in peak noise levels along downstream radiating angles, when forced in the frequency range,  $0.8 \leq St \sim 1.5$ . Although the duty cycle (percentage of the time period of forcing when LAFPA is on) is an additional parameter, Speth & Gaitonde (2013) observe that the response of the jet is less sensitive to this parameter between values of 50% and 90%. They also report that a jet forced at 100% duty cycle behaved identical to the baseline jet.

The placement of LAFPAs around a circular nozzle edge enables the activation of several three-dimensional (3-D) features in the shear layer, depending on the azimuthal modes excited. Each mode has a characteristic influence on the corresponding acoustic sources, thus generating a different far-field impact of forcing. In circular jets the axisymmetric  $m = 0$  mode forcing can be achieved by synchronized firing of all actuators. Higher azimuthal (helical) or flapping modes in the jet can be introduced using suitable phase differences between adjacent actuators. Azimuthal interactions in the jet shear layer can cause these modes to become unstable and compete with one another for energy, which can be leveraged for the purpose of noise control. When operated at a suitable forcing frequency, exciting higher azimuthal modes could lead to a quieter noise signature. Samimy *et al.* (2009, 2010) demonstrated this concept on a Mach 1.3 circular jet, where peak far-field overall sound pressure levels (OASPL) reduced with forcing at higher azimuthal modes. Corresponding computations (Speth & Gaitonde 2013; González, Gaitonde & Lewis 2015) report the production of rollers and braid-like structures with  $m = 0$  forcing, and single and double helical vortical structures with  $m = 1/2$  forcing. These studies concluded that successful noise reduction can be achieved by controlling the size of the structures and restricting their spatial extent of development.

Compared with insights provided by the above literature on control of axisymmetric jets, we currently have little information on the fundamental nature of the shear layer response of rectangular jets to LAFPA-based actuation. Existing works include experimental studies on mixing characteristics of a LAFPA-controlled single jet (Snyder 2007), and more recent works on noise and coupling in twin jets (Ghassemi Isfahani, Webb & Samimy 2021a,b,

2022; Leahy *et al.* 2022; Webb *et al.* 2022; Samimy *et al.* 2023). Other efforts include that of Brès *et al.* (2021), which uses a volumetric heating model to study the action of plasma actuators in a groove on twin rectangular jets, and that of Yeung & Schmidt (2023), which looks at nonlinear triadic interactions in rectangular twin jets forced at its screech frequency. It highlights the effectiveness of LAFPA in reducing the size of large-scale structures using high-frequency excitation, and increasing their three-dimensionality using various forcing patterns, eventually reducing near-field pressure fluctuations and far-field noise. In line with this, our recent computational effort (Lakshmi Narasimha Prasad & Unnikrishnan 2023*b*) detailed the impact of LAFPA-based actuators on rectangular supersonic jets, and identified spectral bands that can result in sound mitigation, which is the first influential control parameter for these actuators. The present work builds on that effort, focusing on the following aspects that are motivated by the second control parameter, the circumferential pattern of forcing along the periphery of the nozzle cross-section.

- (i) What is the 3-D nature of the instabilities excited, and how do they evolve nonlinearly in rectangular shear layers, when utilizing specific actuation patterns informed by dynamics of axisymmetric jets?
- (ii) What are the implications of enhanced three-dimensionality in the excited shear layer structures, for the acoustic response of the plume?
- (iii) How do these subtle changes in the acoustic response translate to the desired far-field noise signature?

To systematically answer these questions, we design controlled simulations on a well-validated baseline rectangular jet, which is forced using LAFPA-based actuators that excite predetermined modes.

Since the study focuses on flow variations triggered by small-perturbation dynamics, we adopt a high-order framework to simulate the baseline and controlled jets, as described in § 2. In addition to the baseline case, we evaluate six modes of forcing, informed by corresponding experiments listed above. These are detailed in § 3. Due to the low AR of the jet studied here ( $AR = 2 : 1$ ), we can draw parallels between the near-field response to these forcing modes and the azimuthal modes of an axisymmetric jet. This interpretation is primarily motivated by the fact that redistributing energy into higher azimuthal modes is beneficial to far-field noise reduction, since progressively higher helical modes are poor acoustic radiators (Michalke & Fuchs 1975). Recent evaluation of rectangular jets of AR up to  $8 : 1$  have also shown that their asymmetric near-field and far-field acoustic signatures can be efficiently represented using the leading few azimuthal Fourier modes (Chakrabarti, Gaitonde & Unnikrishnan 2021).

Following a linear analysis (§ 4) that confirms the receptivity of the shear layer to the choice of forcing frequency, a detailed analysis is presented on the effect of forcing on the mean flow and turbulent statistics (§ 5). Following this, the spatial and spectral imprints of forcing on the near field is discussed in § 6, which are key to understanding the implications of using unsteady actuators for far-field noise of the controlled jets. The near-field acoustic component is specifically analysed in detail in § 7, in the context of its ability to radiate sound into the far field. This can be interpreted as a link between the manipulated shear layer hydrodynamic instabilities and the far-field noise signatures of the controlled jets. Finally, § 8 quantifies the noise mitigation achieved in the far field, and juxtaposes it with the causal fundamental changes materialized in the near-field acoustic component through the chosen forcing modes.

## 2. Numerics

### 2.1. Implicit large eddy simulations

The current effort adopts a high-order simulation framework that solves the 3-D Navier–Stokes equations (NSE) in orthogonal curvilinear coordinates, using an implicit large eddy simulation (ILES) approach. The governing equations in strong conservative form are

$$\frac{\partial}{\partial \tau} \left( \frac{\mathbf{Q}}{J} \right) = - \left[ \left( \frac{\partial \mathbf{F}_i}{\partial \xi} + \frac{\partial \mathbf{G}_i}{\partial \eta} + \frac{\partial \mathbf{H}_i}{\partial \zeta} \right) + \frac{1}{Re} \left( \frac{\partial \mathbf{F}_v}{\partial \xi} + \frac{\partial \mathbf{G}_v}{\partial \eta} + \frac{\partial \mathbf{H}_v}{\partial \zeta} \right) \right], \quad (2.1)$$

where  $\mathbf{Q} = [\rho, \rho u, \rho v, \rho w, \rho E]^T$  is the conserved variables vector,  $(u, v, w)$  are velocity components in the Cartesian coordinate system and  $\rho$  is density. Here  $E = T/[\gamma(\gamma - 1)M_j^2] + (u^2 + v^2 + w^2)/2$  is the total specific internal energy, where  $\gamma$  is the ratio of the specific heats and  $T$  is temperature. The reference Mach number,  $M_j = 1.5$ , is the Mach number at the nozzle exit for this ideally expanded jet. Jacobian of the coordinate transformation is defined as  $J = \partial(\xi, \eta, \zeta)/\partial(x, y, z)$ , where  $(x, y, z)$  and  $(\xi, \eta, \zeta)$  are the Cartesian and computational coordinates, respectively. Inviscid fluxes are denoted by  $(\mathbf{F}_i, \mathbf{G}_i, \mathbf{H}_i)$ , and the viscous fluxes are denoted by  $(\mathbf{F}_v, \mathbf{G}_v, \mathbf{H}_v)$ , along the computational coordinates,  $(\xi, \eta, \zeta)$ , respectively. The ideal gas law,  $p = \rho T/\gamma M_j^2$ , is used to close this set of equations, and a constant Prandtl number,  $Pr = 0.72$ , is assumed. Temperature dependence of viscosity is modelled using Sutherland’s law. Further details of the formulation are available in Garmann (2013).

In the following, a superscript (\*) is used to denote dimensional variables. All primitive variables are non-dimensionalized by their corresponding values at the jet exit except for pressure. Here  $p = p^*/\rho_j^* U_j^{*2}$  is the convention used to non-dimensionalize pressure. The equivalent diameter,  $D_{eq}^* = \sqrt{(4/\pi) \times A_{exit}^*} = 0.758$  in (19.25 mm), defines the diameter of a circular nozzle with an exit area the same as that of the rectangular nozzle, where  $A_{exit}^*$  is the area of the rectangular nozzle exit;  $D_{eq}^*$  is adopted as the reference length scale. Based on  $D_{eq}^*$ , the Reynolds number is defined as  $Re = \rho_j^* U_j^* D_{eq}^* / \mu_j^* \sim 1.09 \times 10^6$ . Here  $T_C^* = D_{eq}^* / U_j^*$  is the characteristic time scale, and non-dimensional time is defined as  $t = t^* / T_C^*$ . The non-dimensional frequency, Strouhal number, is defined as  $St = f^* D_{eq}^* / U_j^*$ , where  $f^*$  is the dimensional frequency in hertz.

A seventh-order weighted essentially non-oscillatory (Liu, Osher & Chan 1994) reconstruction and the Roe scheme (Roe 1981) are used to evaluate inviscid fluxes. Second-order central difference is used to calculate viscous fluxes. Time integration is performed using a nonlinearly stable third-order Runge–Kutta scheme (Shu & Osher 1988). The solver has been extensively validated through prior efforts related to free-shear (Lakshmi Narasimha Prasad *et al.* 2022) and boundary layer (Khobragade, Unnikrishnan & Kumar 2022) flows.

For ILES time integration, a non-dimensional time step defined as  $\Delta t = \Delta t^* / T_C^* = 5 \times 10^{-4}$  is used. Two hundred characteristic time units are used to acquire the temporal evolution of the flow field at a sampling rate of  $St = 20$ . Multiple data sampling durations were used to confirm that this was sufficient for the convergence of first- and second-order statistics in the turbulent plume, and far-field acoustics. Integration of power spectral density between  $0.05 \leq St \leq 1.5$  is used to obtain OASPL.

The computational domain consists of approximately  $48 \times 10^6$  nodes, with 511 nodes in the streamwise direction, 301 nodes along the longer side and 309 nodes along the

shorter side of the rectangular nozzle, respectively. This results in a physical domain of approximately  $30D_{eq}$  in the streamwise direction and  $12D_{eq}$  in the other two orthogonal directions. Near the nozzle walls and exit, grid refinement is provided with a minimum wall-normal spacing of  $\Delta n \sim 0.001$ . The transverse grid spacing near the shear layer is  $\Delta y, \Delta z \sim 0.001$ , while the typical streamwise grid spacing in the plume is  $\Delta x \sim 0.025$ . The grid is gradually stretched toward the outflow boundaries to avoid numerical reflections into the domain. These grid parameters are informed by previous studies of similar compressible rectangular jets (Gojon, Gutmark & Mihaescu 2019; Chakrabarti *et al.* 2021).

### 2.2. Navier–Stokes based mean flow perturbation

To control the shear layer dynamics of the rectangular jet, the actuation needs to incite instabilities to which the near-nozzle flow is receptive. One way to identify the relevant spectral band of actuation is to evaluate the linear tendencies of the shear layer, which can be obtained from the solution of the linearized governing equations, about the time-averaged basic state of the baseline jet. We adopt the Navier–Stokes based mean flow perturbation (NS-MFP) approach to solve the linearized form of (2.1), which has been detailed in Ranjan, Unnikrishnan & Gaitonde (2020); Ranjan *et al.* (2021). The NS-MFP approach effectively solves the linear evolution of perturbations over a basic state, by utilizing a body force constraint on the nonlinear NSE. Due to the above constraint, the basic state need not be a laminar solution of the NSE. The action of NS-MFP can be represented as

$$\frac{\partial \mathcal{Q}'}{\partial t} = \left[ \frac{\partial F(\bar{\mathcal{Q}})}{\partial \bar{\mathcal{Q}}} \right] \mathcal{Q}', \quad \left[ \frac{\partial F(\bar{\mathcal{Q}})}{\partial \bar{\mathcal{Q}}} \right] = A(\bar{\mathcal{Q}}). \quad (2.2)$$

In the above,  $\mathcal{Q}'$  is the linear perturbations in the conserved variables,  $\bar{\mathcal{Q}}$  is the basic state chosen for the linear analysis and  $A(\bar{\mathcal{Q}})$  is the Jacobian representing the spatial operations in the linearized operator. Further details on the basic state and perturbations will be provided in the context of linear analysis results in § 4.

### 3. Simulation parameters

This study focuses on control of a Mach 1.5 jet exiting a rectangular nozzle. The nozzle has an AR of 2 : 1, with dimensions of 0.950 inches (24.13 mm) along the longer edge and 0.475 inches (12.06 mm) along the shorter edge. These dimensions are identical to those reported in Isfahani, Webb & Samimy (2021). The nozzle is modelled as a constant area sleeve of streamwise length,  $3.64D_{eq}$ , as shown in figure 1(a). The bisecting plane perpendicular to the shorter edges of the nozzle is referred to as the major axis plane, while the bisecting plane perpendicular to the longer edges of the nozzle is referred to as the minor axis plane as seen in figure 1(b). The grey regions in figure 1(b) constitute the nozzle block, which are excluded from the fluid domain. Here  $x$  corresponds to the streamwise direction, and  $y$  and  $z$  correspond to the transverse directions parallel to the shorter and longer edges of the nozzle, respectively. The centroid of the rectangular section at the nozzle exit plane is the origin of this Cartesian coordinate system.

The jet is operated at a perfectly expanded condition with a nozzle pressure ratio (ratio of stagnation pressure,  $p_o^*$ , to ambient pressure) of 3.67. The jet exit velocity is  $u_{jet}^* = 424.74 \text{ m s}^{-1}$ . This unheated jet has a static temperature of  $T^* = 224 \text{ K}$ , and exits to ambient conditions of  $T_\infty^* = 300 \text{ K}$  and  $p_\infty^* = 101.325 \text{ kPa}$ . In order to implement

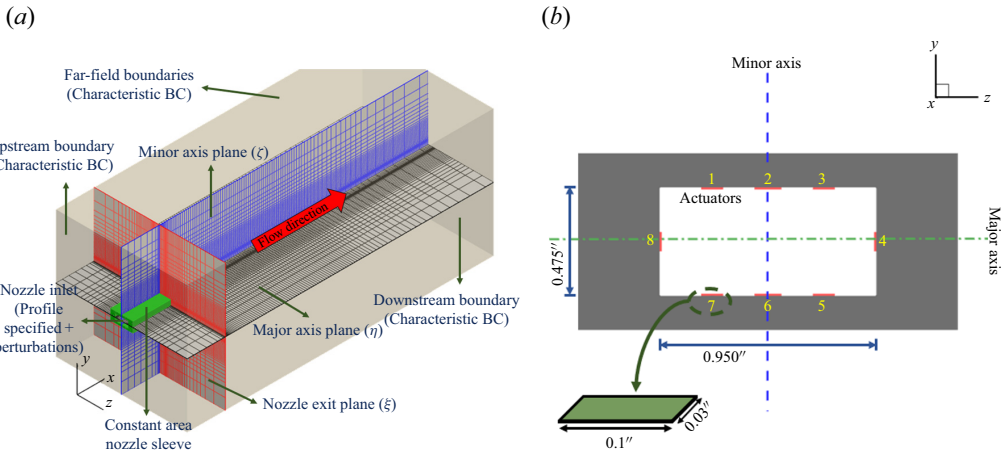


Figure 1. (a) Principal planes of the computational domain and applied boundary conditions. Every fourth node is shown. (b) Schematic of the nozzle and actuators. Nozzle and actuator dimensions, and principal planes are also shown.

characteristic boundary conditions in a robust manner, a small velocity ( $u_{\infty}^* = 0.01 \times u_{jet}^*$ ) (Birch *et al.* 2005) is imposed on the ambient flow outside the nozzle. The boundary conditions used on the computational domain have been highlighted in figure 1(a). Non-reflecting characteristic boundary conditions (Poinsot & Lele 1992; Blazek 2001) are applied to upstream boundaries outside the nozzle and far-field boundaries. Along with grid stretching, the order of reconstruction is locally lowered at the outer boundaries to reduce reflections. Nozzle surfaces are treated as adiabatic no-slip walls. At the inlet of the nozzle block, Dirichlet inflow conditions are imposed similar to Bogey & Bailly (2010). Boundary layer thickness typical of these high-speed compressible jets from experimental estimates by Samimy *et al.* (2007a) is  $\delta_{99}^* \sim 1$  mm. Therefore, velocity and density profiles with  $\delta_{99}^* \sim 0.85$  mm are imposed at the nozzle inlet. Spatio-temporally correlated ‘coloured’ pressure perturbations (Adler *et al.* 2018) are imposed on the boundary layer and are allowed to evolve across the length of the nozzle sleeve before exiting into the ambient to aid the formation of stochastic perturbations in the shear layer. As a result, the boundary layer, and subsequently the shear layer, have a broadband spectral nature. The boundary layer at the exit of the nozzle block has a displacement thickness of  $\delta^D \sim 0.01635D_{eq}$ , momentum thickness,  $\theta \sim 0.00675D_{eq}$ , and shape factor,  $H = \delta^D/\theta \sim 2.422$ .

The simulation of the baseline jet corresponding to the above parameters was extensively validated using published experimental and computational results in Lakshmi Narasimha Prasad & Unnikrishnan (2023b). These results are omitted for brevity. Its grid convergence was also ensured in the above work, and the results reported here are obtained on the grid detailed in § 2.

In the controlled simulations, the LAFPA actuator is modelled as a surface heating element based on past computational studies (Gaitonde & Samimy 2011). In this study we model eight actuators around the periphery of the nozzle inner wall close to the exit plane, as shown in figure 1(b). Three actuators are placed equidistant from each other and the nozzle walls along the longer edges. One actuator is placed at the centre of the shorter edges as well. Each actuator has dimensions of 0.1" (2.5 mm)  $\times$  0.03" (0.75 mm) ( $l \times b$ ). The centre of each actuator is located 0.0569" (1.44 mm) from the nozzle exit.

	Forcing frequency ( $St$ )	Duty cycle (%)	Phase difference
Baseline	—	—	—
Control M0	1	50	0
Control M1	1	50	$\pi/4$
Control M2	1	50	$\pi/2$
Control M3	1	50	$3\pi/4$
Control $M\pi$	1	50	$\pi$
Control $M+/-1$	1	50	$\pi$ (grouped)

Table 1. Baseline and controlled cases studied in the present work.

The arrangement and physical dimensions of the LAFPA actuators are consistent with experimental parameters (Isfahani *et al.* 2021) and prior computational models (Gaitonde 2012). In line with spectroscopic temperature readings from the experiments (Samimy *et al.* 2009; Gaitonde & Samimy 2010), the local surface temperature rises to  $T = 5T_j$  when the actuators are on. This Dirichlet condition for temperature, no-slip conditions on velocity components, homogeneous Neumann condition on pressure and ideal gas law for density, provide the necessary closure for the governing equations on the actuator surface.

As identified in § 1, the key objective here is to study the nature of 3-D structures excited by LAFPA in rectangular shear layers, and their acoustic impact. Towards this end, we select a suitable frequency and duty cycle of excitation, and forcing sequences as identified in table 1. The choice of forcing frequency ( $St = 1$ ) is based on the linear analysis of the shear layer, which will be discussed next in § 4. The duty cycle refers to the percentage of a time period of actuation, during which the actuators are on. The duty cycle is chosen based on prior computations on circular jets (Speth & Gaitonde 2013; González *et al.* 2015), where control authority of LAFPAs was found to increase with the duty cycle at lower values, but saturated beyond DC  $\sim 50\%$  (where ‘DC’ denotes ‘duty cycle’). The forcing sequences are named based on the similarities between the near-field response of the controlled rectangular jets and corresponding patterns in a circular jet (Samimy *et al.* 2008; Gaitonde & Samimy 2010). For example, the M0 forcing results in all the actuators firing in tandem (similar to axisymmetric forcing in a circular jet), while the M1, M2, M3 and  $M\pi$  forcings have increasing phase lags between successive actuators, creating a helical pattern (corresponding to the first or higher azimuthal modes in a circular jet). The  $M+/-1$  forcing corresponds to the flapping mode of the rectangular jet (as seen on the minor axis plane), where the group of actuators on the two longer edges of the nozzle fire with a phase difference of  $\pi$  between them. These forcing patterns are informed by experimental implementation in the references cited above.

For additional clarity on the forcing patterns, we present the temporally varying temperature signals imposed on the eight actuators in figure 2. In these figures the abscissa represents actuator number, while the ordinate represents non-dimensional time. The contour levels shown in these figures represent non-dimensional temperature ( $T = T^*/T_{jet}^*$ ). For the  $St = 1$  forcing, there is one actuation per unit non-dimensional time. Here DC = 50% indicates that the actuators are on for 50% of each actuation cycle and off for the rest. The M0 forcing (figure 2a) is achieved by having all eight actuators fire in synchronization without any phase difference between them. The M1 forcing (figure 2b) has a phase difference of  $\pi/4$  between adjacent actuators. The M2 forcing (figure 2c) has a phase shift of  $\pi/2$  between adjacent actuators with two ‘diametrically’ opposite actuators firing in phase. The M3 forcing (figure 2d) has a phase shift of  $3\pi/4$ , while the  $M\pi$  forcing



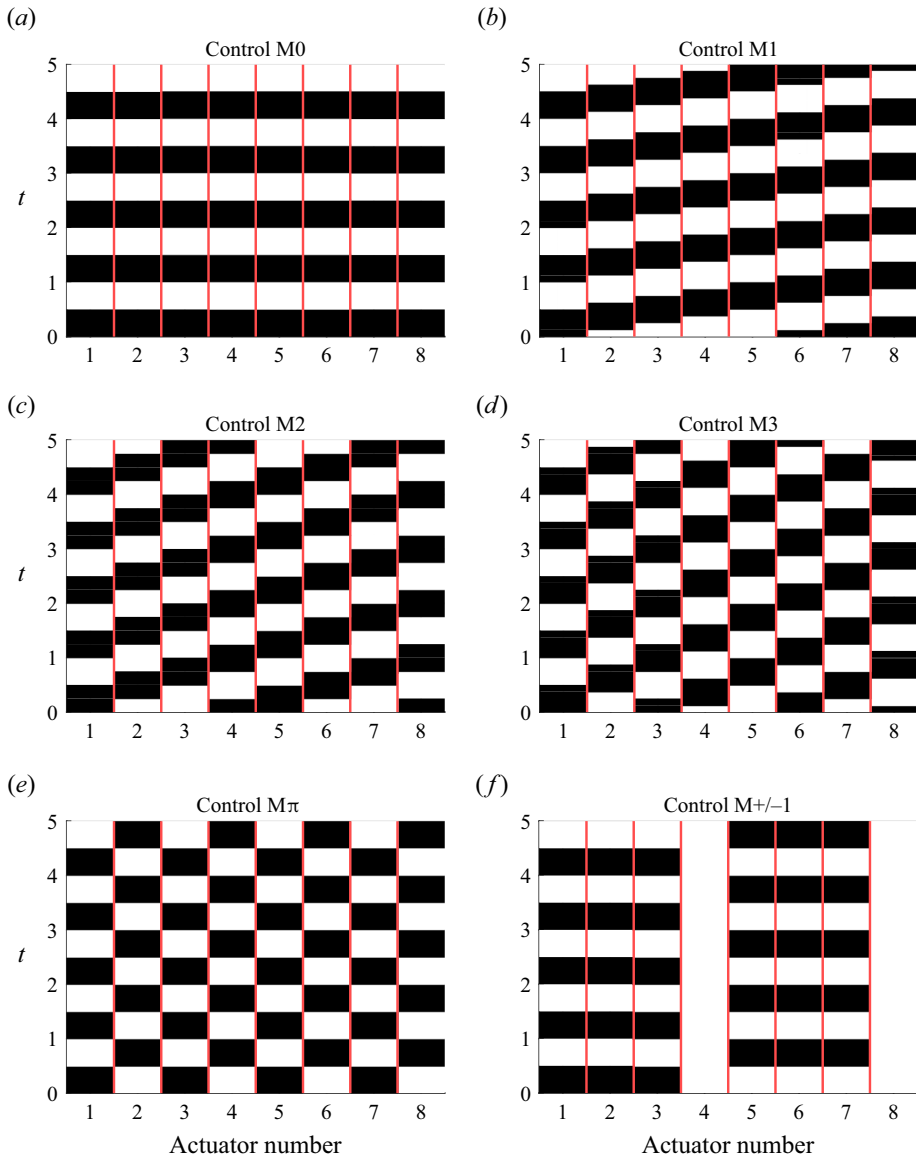


Figure 2. Temperature value imposed on each of the eight actuators. (a) The M0 forcing, (b) M1 forcing, (c) M2 forcing, (d) M3 forcing, (e)  $M\pi$  forcing and (f)  $M+/-1$  forcing. Black and white patches correspond to time segments where each actuator is on ( $T = 5$ ) and off ( $T = 1$ ), respectively.

(figure 2e) has a phase shift of  $\pi$ . In  $M+/-1$  forcing (figure 2f), the three actuators along a longer edge of the nozzle fire in phase, while the set of actuators on the opposite edge fire at a phase difference of  $\pi$ . The actuators on the shorter edge are not turned on for this case.

A representative temperature signature of an actuator functioning at DC = 50% is shown in figure 3(a). To quantify the spectral excitation achieved by the actuator signal, figure 3(b) plots the normalized power spectral density of the forcing signal applied at the actuators. It is evident that the primary frequency with the largest amplitude is  $St = 1$ .

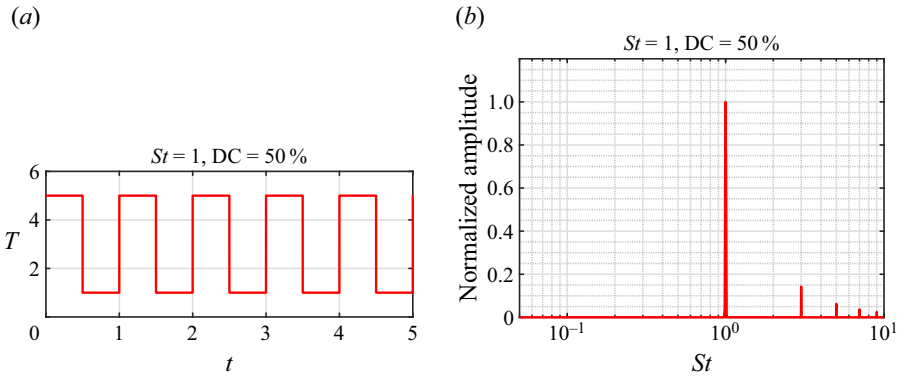


Figure 3. (a) Temporal variation of the temperature at the location of the actuators. (b) Power spectral density of the forcing signal.

Odd harmonics ( $St = 3$ ,  $St = 5$ , etc.) of the fundamental forcing are also excited at this duty cycle, albeit at lower energy levels. The amplitude of the superharmonic at  $St = 3$  is about 15 % of the fundamental. Subsequent superharmonics have amplitudes that are less than 5 % of the fundamental, and are hence expected to have minimal impact on the flow.

Among the controlled cases chosen here, the hydrodynamic and acoustic responses of the jet displayed minimal variations beyond a phase difference of  $\pi/2$  between adjacent actuators. Therefore, in the interest of brevity, following sections will examine M0, M1, M2 and M+/-1 forcing cases in detail. For completeness, key results from the M3 and  $M\pi$  forcing cases are summarized in [Appendix A](#).

#### 4. Linear response of the flow

To identify the jet's spectral range of sensitivity in the vicinity of the nozzle exit, we subject the mean flow field of the baseline simulation to linear perturbation analysis. For simplicity, we present a two-dimensional analysis, where the basic states on the two principal planes are extracted from the 3-D time-averaged ILES flow field. While a linear analysis is strictly applicable only to the laminar basic state, such studies when performed on time-averaged turbulent flows can provide key insights into the spatio-temporal scales of relevance in the flow (Sun *et al.* 2017; Ranjan *et al.* 2021). We also neglect the effect of eddy viscosity on the linear evolution of perturbations in the shear layer, following the approach in Bhaumik *et al.* (2018). To obtain the basic states, the baseline simulation is time averaged for 200 characteristic time units. Due to the convective nature of instabilities in this shear layer, a continuous white noise forcing is utilized in the linear simulations. The perturbations are applied within the nozzle block at a distance of  $0.5D_{eq}$  upstream of the nozzle exit, and at a distance of  $0.1D_{eq}$  from the nozzle walls. To ensure linearity of the results, the root-mean-square amplitude of the forcing is limited to  $O(10^{-7})$ .

The results are presented in [figure 4](#) for both the principal planes. The basic states are represented using streamwise velocity contours in [figure 4\(a,b\)](#). The corresponding linear pressure perturbation spectra along the lip line (dashed lines in [figure 4a,b](#)) are plotted in [figure 4\(c,d\)](#). The lip line corresponds to the horizontal line with the  $z$  and  $y$  coordinate equal to that of the inner surface of the nozzle on the major and minor axis planes, respectively. This helps identify the most linearly amplified frequency in the near-nozzle shear layer. Dominant spectral peaks are observed at  $St \sim 1$  and at  $St \sim 0.85$  on the major

## Noise mitigation in rectangular jets

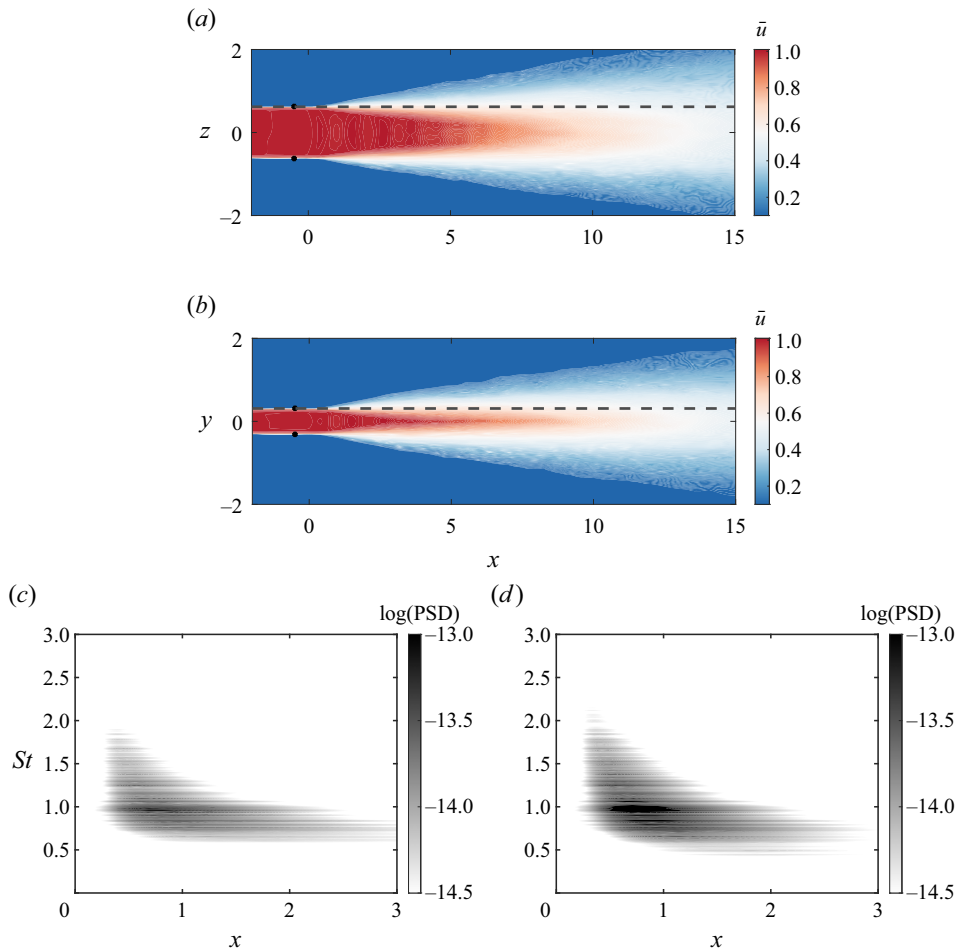


Figure 4. Mean axial velocity contours on (a) major axis plane and (b) minor axis plane used as basic states for NS-MFP studies. Velocity is normalized by its corresponding value at the nozzle exit. Black dots represent the location where the random white noise forcing is introduced. Streamwise variation of the logarithm of the power spectral density of pressure fluctuations along the jet lip line (dashed line) on the (c) major axis plane and (d) minor axis plane.

axis plane, indicating that the shear layer could be highly receptive to LAFPA-based control in this spectral vicinity. The shear layer on the minor axis plane also displays spectral peaks at  $St \sim 1$  and at  $St \sim 0.8$ .

The streamwise linear amplification at specific frequencies is quantified in figure 5 using the N factor, defined as the logarithm of the ratio of perturbation energy at a given  $x$  location to its energy at a reference position,  $x_o$ . The reference position chosen to calculate the N factor is the streamwise location of the forcing,  $x = -0.5D_{eq}$ . The N factor curves for various frequencies between  $0.8 \leq St \leq 2.5$  on the major and minor axis planes are shown in figure 5(a,b). Although peak N factors vary slightly between the two planes (largely due to the difference in spreading characteristics of the shear layers), the relative trend among various frequencies are consistent. The highest N factor of  $\sim 7$  is achieved at  $St = 1$  ( $St_\theta = 0.0068$ ) on both planes, consistent with the amplification noted in the spectra in figure 4(c,d). Here  $St_\theta$  is the non-dimensional frequency in terms of Strouhal number

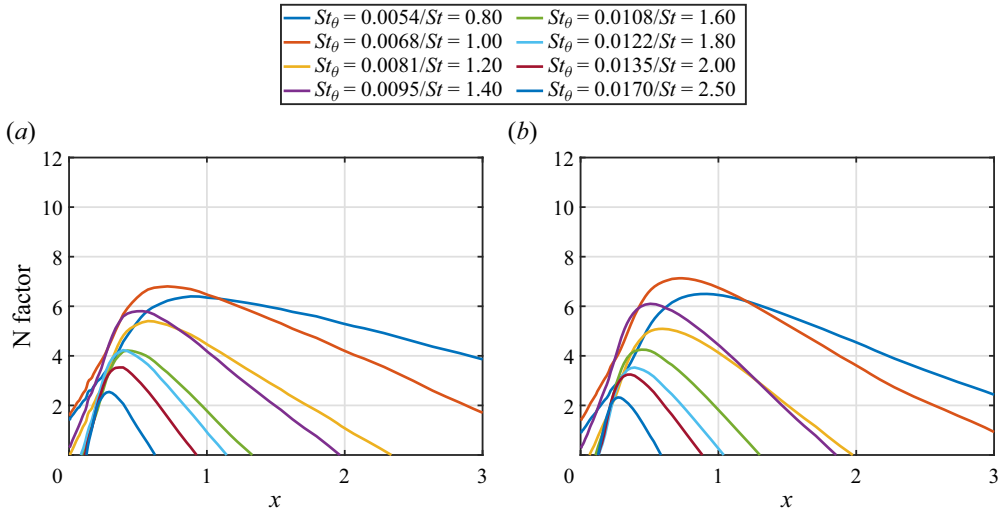


Figure 5. Streamwise variation of the N factor along the jet lip line on the (a) major axis plane and (b) minor axis plane.

scaled with the exit momentum thickness of the nozzle boundary layer. This is consistent with the dominant shear layer spectrum for the thin boundary layer of a Mach 1.5 circular jet, reported by Bogey (2022). On both planes, the peak N factor decreases with increasing frequencies. The N factors indicate that perturbation amplification is about 3 to 4 orders of magnitude higher at  $St = 1$  ( $St_\theta = 0.0068$ ), when compared with that at the higher end of the spectrum, e.g.  $St = 2$  ( $St_\theta = 0.0135$ ). In addition to the higher peak value of the N factor,  $St = 1$  has a longer streamwise region of amplification within the shear layer. This suggests that the associated instabilities have a longer region of residence in the shear layer, and could potentially impact the nonlinear evolution of coherent structures (excited at these frequencies) more effectively than higher frequencies. Conversely, the higher frequencies ( $St \sim 2$  and above) saturate closer to the nozzle exit, as the spreading shear layer becomes less receptive to this spectral range. These observations are also consistent with prior nonlinear simulations (Lakshmi Narasimha Prasad & Unnikrishnan 2023b) that have identified  $St \sim 1$  as a suitable frequency to perturb this shear layer.

### 5. Effect of actuation on flow statistics

In this section we detail the variations induced in the first- and second-order statistical properties of the controlled jets, when actuated using various forcing sequences as defined in table 1.

#### 5.1. Mean flow

When utilizing small-perturbation-based noise control techniques, it is advantageous to achieve the desirable acoustic modifications without significantly affecting the mean flow. Changes to the mean flow caused by control are relevant to noise modelling studies (Rosa 2018; Prasad & Gaitonde 2022), practical aspects of scalability (Brown 2008) and performance characteristics such as the thrust generated by the nozzle (Prasad & Morris 2021; Liu *et al.* 2022). Therefore, to understand the effects of control on the mean flow, we

## Noise mitigation in rectangular jets

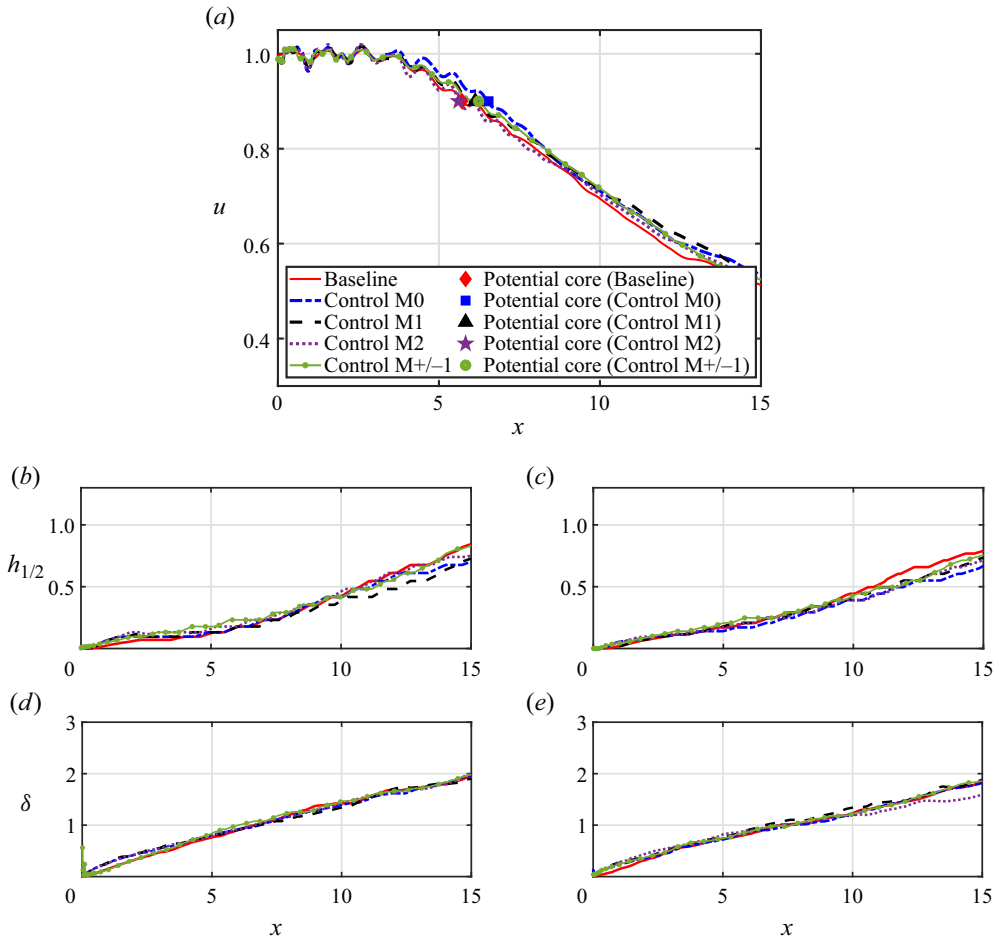


Figure 6. (a) Centreline velocity comparison between baseline and controlled cases. Potential core collapse locations are also shown. Half-width comparison on the (b) major axis plane and (c) minor axis plane. Streamwise variation of shear layer thickness on the (d) major axis plane and (e) minor axis plane.

compare parameters including centreline velocity, core collapse location, spreading rate and shear layer thickness, with the baseline jet, as shown in figure 6.

Centreline velocity comparison among various cases (figure 6a) shows very small differences. The end of the potential core for each case is also indicated in figure 6(a), based on the definition by Georgiadis & Papamoschou (2003). This is the axial location where streamwise velocity reaches 90% of the nozzle exit velocity. The potential core lengths are also quantified in table 2. The controlled cases, M0, M1 and M+/-1 display a slight increase in potential core length (suggesting a slower decay rate). The M0 forcing results in the largest variation in the mean flow, where the potential core is  $\sim 14.5\%$  more than that in the baseline. This is consistent with the excitation of circumferentially correlated energetic coherent structures that are most capable of modifying the mean flow. The M2 forcing results in minimal variation in the potential core length, compared with the baseline case.

Spreading rate comparison is shown in figure 6(b,c) on the major and minor axis planes, respectively, by plotting the half-width ( $h_{1/2}$ ) of the jets. The baseline and controlled jets

Baseline	Control M0	Control M1	Control M+/-1	Control M2
5.71	6.54	6.21	6.31	5.62

Table 2. Potential core lengths (in units of  $D_{eq}$ ).

exhibit similar spreading rates until the collapse of the potential core ( $x \sim 6$ ). Downstream of the potential core, the control decelerates spreading, indicating a slower rate of ambient fluid entrainment. This is consistent with the findings of Huet *et al.* (2009), which revealed reduced centreline velocity decay rates for circular jets that were forced with pulsed micro-jets. The major axis plane has relatively more variations in half-widths, with M1 forcing exhibiting the slowest growth rate.

Streamwise variation of shear layer thickness ( $\delta$ ) on the principal planes of the nozzle are plotted in figure 6(d,e). The (transverse coordinate) extent bounding streamwise velocity between 10 % and 90 % of the centreline velocity is used to calculate shear layer thickness (Papamoschou & Roshko 1988). In general, the production of coherent vortices as a result of actuation (detailed in the subsequent section) leads to localized thickening of the shear layer near the nozzle exit for all the controlled jets. This is observed on both planes for M0, M1 and M2 forcings. However, M+/-1 forcing shows this behaviour only on the minor axis plane, since the actuators on the shorter edges of the nozzle are inactive in this case, as detailed in § 3. Therefore, on the major axis plane, the shear layer in the M+/-1 forcing is almost identical to that in the baseline case. Downstream of  $x \sim 2.5$ , the shear layer thickness of all the jets are almost identical on both planes. This indicates that the vortical impact of actuation is primarily localized to around  $2.5D_{eq}$  from the nozzle exit.

Overall, these results indicate that for the forcing parameters tested in the current study, the effect of actuation on mean flow quantities is relatively minor. The largest relative deviation from the baseline case is seen for the M0 forcing sequence. Higher modes of forcing progressively shift the mean flow trends towards the baseline jet, since they are less likely to sustain large-amplitude energetic coherent structures that distort the time-averaged basic state.

### 5.2. Turbulent statistics

The effects of actuation on fluctuating scales are evaluated by performing a budget of turbulent kinetic energy (TKE) at the jet inner lip line. Since the nozzle principal planes intersect at least one actuator, TKE variation along the inner lip line characterizes the direct impact of actuation on the turbulent statistics of the jet. Turbulent kinetic energy is defined as

$$\text{TKE} = \frac{1}{2}(\widetilde{u'^2} + \widetilde{v'^2} + \widetilde{w'^2}), \tag{5.1}$$

where  $q'' = q - \tilde{q}$  represents Favre fluctuations of a quantity,  $q$ , while  $\tilde{q}$  represents the corresponding Favre average.

Figure 7(a,b) shows the variation of TKE at the nozzle inner lip line on the major axis plane and minor axis plane, respectively, for the baseline and controlled jets. The baseline jet has relatively small yet finite levels of TKE inside the nozzle, contributed by the coloured pressure perturbations imposed at the inflow. Outside the nozzle, the shear layer instabilities intensify mixing, and significantly increase the TKE. As the shear layer

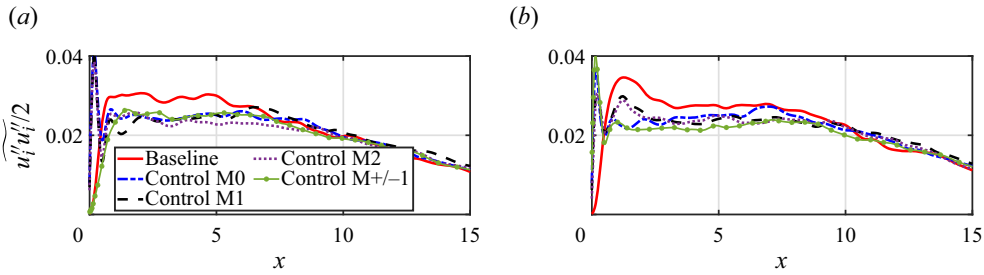


Figure 7. Streamwise variation of turbulent kinetic energy (TKE) at the nozzle inner lip line on the (a) major axis plane and (b) minor axis plane.

spreads entraining ambient fluid, TKE levels attain an equilibrium value, until the core collapse location. Following core collapse, TKE levels decrease in a quasi-linear fashion.

The controlled jets exhibit a high concentration of TKE near the nozzle exit, as a result of actuation. While this is seen on both planes for M0, M1 and M2, the M+/-1 forcing has a TKE peak only on the minor axis plane (since the actuators bisecting the major axis plane are not activated). Following the near-actuator peak, TKE values fall to levels lower than in the baseline, till the core collapse location. Beyond the end of the potential core, TKE levels in the controlled jets are comparable to that in the baseline jet. These trends suggest that the effect of actuation on turbulent fluctuations is most evident in the spreading zone of the shear layer. An interesting observation with the M+/-1 forcing is that, despite the actuators being deactivated on the shorter edges of the nozzle, TKE reduction achieved on the major axis plane is at par with that in the other controlled cases. This could be due to the coupled dynamics between shear layers emerging from the longer and shorter edges of the nozzle.

The reduction in TKE seen in the controlled jets can be attributed to two mechanisms, based on the analysis of the TKE budget equation (not included for brevity): (a) reduction in TKE production within the post-actuation zone of the shear layer primarily due to lower Reynolds stresses, and (b) increased TKE convection levels upstream of the core collapse (Lakshmi Narasimha Prasad & Unnikrishnan 2023c), aiding in efficient redistribution of peak TKE levels.

## 6. Near-field response to actuation

The controlled jets display unique near-field vortical and acoustic responses to various modes of actuation. These differences in the fundamental behaviour of shear layers and its acoustic emissions are critical in defining the far-field noise signature of the controlled jets. Here we detail these responses, which will help us better interpret the control authority of various actuation strategies.

### 6.1. Shear layer response

The response of the shear layer highlighting the vortical mechanisms in the controlled jets is first evaluated in figure 8. The phase-averaged Q-criterion coloured by streamwise velocity,  $u$ , are displayed at selected instances of the forcing time period. A time period of the forcing is used as the reference signal for phase averaging of the controlled jets. For comparison, the baseline jet is also included by phase averaging the flow field at  $St = 1$ , starting from the first snapshot collected (since the baseline jet cannot be phase

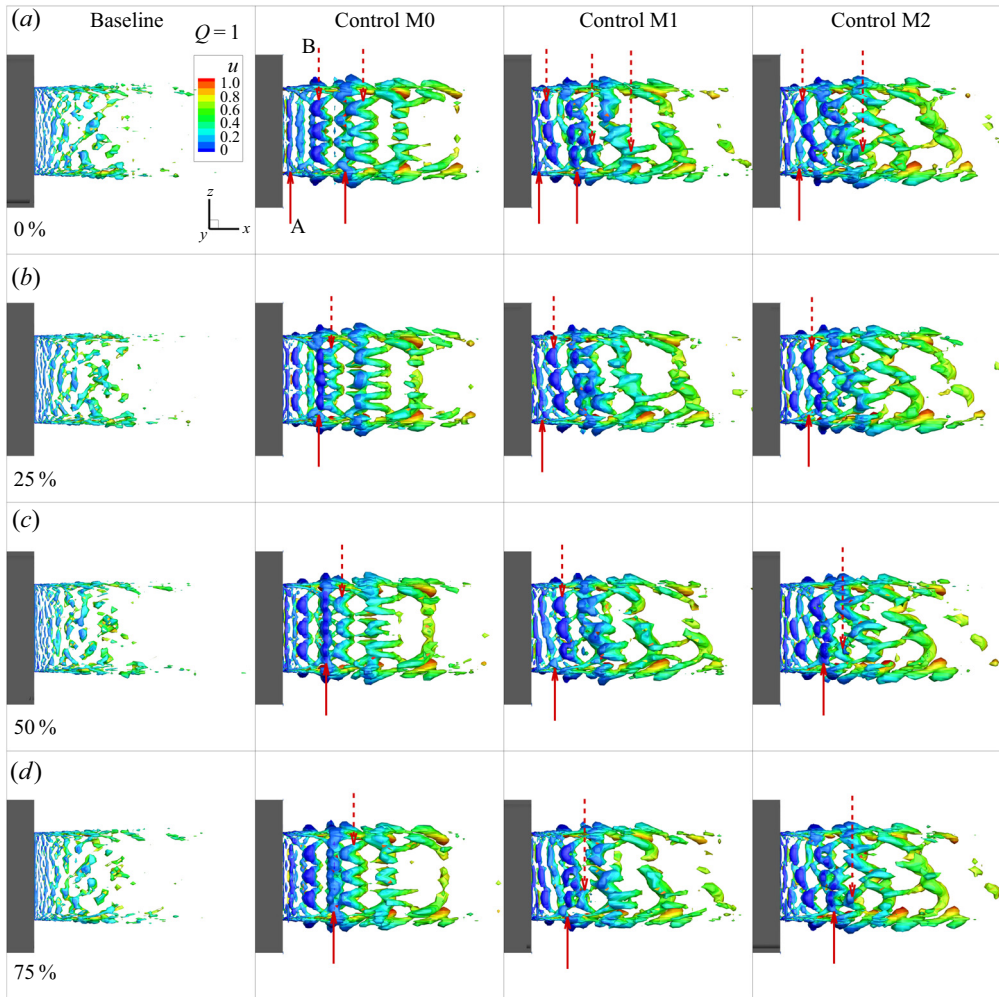


Figure 8. Phase-averaged flow features in the shear layer at indicated phases for the baseline and three forcing cases. The red solid and dashed arrows track vortices generated when an actuator is on and off, respectively.

locked to any particular forcing signal). This first snapshot is collected after the simulation attains statistical stationarity. The columns in figure 8 correspond to baseline, M0, M1 and M2 forcings as indicated. The rows correspond to snapshots of the flow at four representative instances in the forcing cycle,  $0 \leq t_f \leq T_f$ , in terms of percentage of  $t_f/T_f$ . Here  $T_f$  represents the time period of forcing and is defined as  $1/St_f$ , where  $St_f$  is the non-dimensional frequency of forcing. In the controlled shear layers, the upward pointing solid red arrow tracks the vortical structure ‘A’ produced in the shear layer, while the downward pointing dashed red arrow tracks a different vortical structure, ‘B.’ When the actuators turn on at the start of a cycle, the extended vortical element A is created, which is parallel to the shear layer generated from the longer edge of the nozzle. Here B corresponds to structures that are produced when the actuators turn off, which eventually transform into lambda vortices.

Flow features occurring naturally at  $St = 1$  are limited to regions close to the nozzle exit in the baseline jet. In M0 actuation, lambda vortices, B, are stretched in the high-velocity



core, while their ‘head’ region lags in the surrounding ambient fluid, as shown in figure 8(a). These ‘head’ regions later get pinched-off from the streamwise vortices, and interact with the trailing A vortical structure, forming a circumferentially connected element. These interactions result in a staggered pattern of vortices, as visible in the four instances of M0. The M1 actuation also exhibits a similar set of dynamics involving A and B vortical structures. The key difference here is that the lambda vortices and the circumferentially connected elements follow a helical pattern, due to the phase difference imposed on the consecutive actuators. However, the streamwise vortices in M1 is relatively weaker in comparison to M0. In M2 forcing, the streamwise strength of vortical elements are at par with that in M0. Furthermore, it also promotes higher helical modes in the consecutive sets of staggered lambda vortices. In essence, M2 forcing combines the advantages gained in M0 and M1 forcings, by generating stronger streamwise vorticity and higher helical modes. This enhances the 3-D nature of the shear layer response in a way conducive for noise source mitigation (Samimy *et al.* 2023). Phase-averaged response of the shear layer in the  $M+/-1$  forcing is similar to that achieved in the M0 forcing, and thus has been excluded for brevity. The primary difference is that the vortices produced in the upper and lower shear layers (on the longer edges) of the jet are in phase for M0 forcing, while they are out of phase in  $M+/-1$  forcing.

Thus, the vortical effect of forcing on the shear layer is the production of streamwise-elongated lambda vortices, with the degree of three-dimensionality dependent on the mode of forcing. This reinforces the observation in §4 that the shear layer is receptive to the spectrum in the vicinity of  $St = 1$ , resulting in generation of vortices that scale with shear layer thickness. This provides the actuators the control authority necessary to tailor the evolution of coherent shear layer structures, and eventually, its acoustic signature. This is studied in the following section.

## 6.2. Acoustic response

Here we detail the acoustic response to forcing, in the plume and near field of the controlled jets. By near field we refer to the spatial region resolved in the ILES. Since hydrodynamic fluctuations attenuate rapidly in the radial direction from the jet centreline, the acoustic directivity in the near field can be evaluated using the dilatation field (Colonius, Lele & Moin 1997). However, in the plume, the energetic hydrodynamic fluctuations mask the acoustic response of the jet. Therefore, we extract the acoustic response in the plume of the controlled jets using Doak’s momentum potential theory (Doak 1989; Unnikrishnan & Gaitonde 2016).

### 6.2.1. Acoustic response of the plume

The effect of actuation on the acoustically relevant fluctuations of the plume is isolated through a Helmholtz decomposition on the mass flux vector field ( $\rho\mathbf{u}$ ). This segregates its solenoidal (hydrodynamic) and irrotational (acoustic and thermal) components, which can be represented using

$$\rho\mathbf{u} = \bar{\mathbf{B}} + \mathbf{B}' - \nabla(\psi'_a + \psi'_T), \quad (6.1)$$

where  $\bar{\mathbf{B}}$  and  $\mathbf{B}'$  are the mean and fluctuating solenoidal components, respectively;  $\psi'_a$  and  $\psi'_T$  are the irrotational scalar potentials for the acoustic and thermal components, respectively. By utilizing the above relation in the continuity equation, the acoustic and thermal components of the flow can be extracted by solving the following Poisson

equations:

$$\nabla^2 \psi'_a = \frac{1}{c^2} \frac{\partial p}{\partial t}, \quad \nabla^2 \psi'_T = \frac{\partial \rho}{\partial S} \frac{\partial S}{\partial t}. \quad (6.2a,b)$$

Here  $c$  is the local speed of sound and  $S$  is entropy. Additional details of the decomposition are available in Unnikrishnan & Gaitonde (2016). The streamwise component of acoustic fluctuations ( $-\partial \psi'_a / \partial x$ ) mostly determines the downstream radiated noise. Since the control is most effective in manipulating the downstream noise emissions (as will be shown later in § 8), the following discussions will focus on this streamwise component, which will be referred to as  $A_x$ , where  $A_x = (-\partial \psi'_a / \partial x)$ . As shown in Chakrabarti *et al.* (2021), this acoustically filtered component of the flow exhibits a wavepacket behaviour in rectangular jets.

The acoustic response (at the forcing frequency) in the plume is represented using phase-averaged iso-levels of  $A_x$ , as shown in figure 9. The projected views on the major and minor axis planes for the baseline jet are shown in figures 9(a) and 9(b), respectively. Corresponding results for M0 forcing (c,d), M1 forcing (e,f), M2 forcing (g,h) and M+/-1 forcing (i,j) are also included. The baseline jet has a limited acoustic signature at  $St = 1$ , which is restricted to the near-nozzle regions. The M0 forcing results in an axially compact wavepacket, which reflects the AR of the nozzle. The acoustic response to M1 forcing is a helical wavepacket that sustains further downstream. The M2 forcing produces a ‘double helix’, with streamwise extent in between that of the M0 and M1 forcing. As will be evident in the following section, the double helix acoustic wavepacket contains two cycles of azimuthal oscillations at a given streamwise location. These acoustic responses in this low-AR rectangular jet draw a parallel with the responses observed in circular jets, when actuated using various azimuthal modes of LAFPA-based controllers (Gaitonde & Samimy 2010; Gaitonde 2012). In response to M+/-1 forcing, the acoustic wavepacket has an anti-symmetric structure with respect to the major axis plane. This structure is similar to those observed in flapping rectangular jets, e.g. as discussed in Gojon *et al.* (2019). The streamwise extent of this wavepacket is longer than those excited by the other controlled jets. This evaluation demonstrates that the forcing pattern of the actuators has a strong influence on the 3-D form of the acoustic response of the plume.

### 6.2.2. Acoustic directivity

The near-field acoustic response to forcing at  $St = 1$  is shown in figure 10, using phase-averaged contours of dilatation. Response to M0 forcing is represented at the middle of the actuator on phase,  $t_f / T_f = 0.25$ , on the two principal planes of the jet. Two bands of acoustic radiation are produced on the minor axis plane. The dominant band propagates in the downstream direction, and eventually spreads across the propagation plane within  $20^\circ \leq \theta \leq 60^\circ$ , approximately centred around the red solid line. This band is induced by intrusion of vortical structures into the potential core (Unnikrishnan & Gaitonde 2016), which are generated as a nonlinear shear layer response to the forcing (Lakshmi Narasimha Prasad & Unnikrishnan 2023b). The sideline direction ( $70^\circ \leq \theta \leq 90^\circ$ ) is dominated by the second band of acoustic radiation, which is approximately centred around the blue dashed line in figure 10. This appears at the nozzle exit, and is a direct impact of the pressure fluctuations produced by the plasma actuator. While the spatial structure of the second (sideline) radiation band differs on the two principal planes, that of the first (downstream) is similar on both the planes, which is consistent with the above hypothesis. All the control cases studied here have this general form of near-field acoustic response on the principal planes at the forcing frequency. The main difference arises in the M+/-1

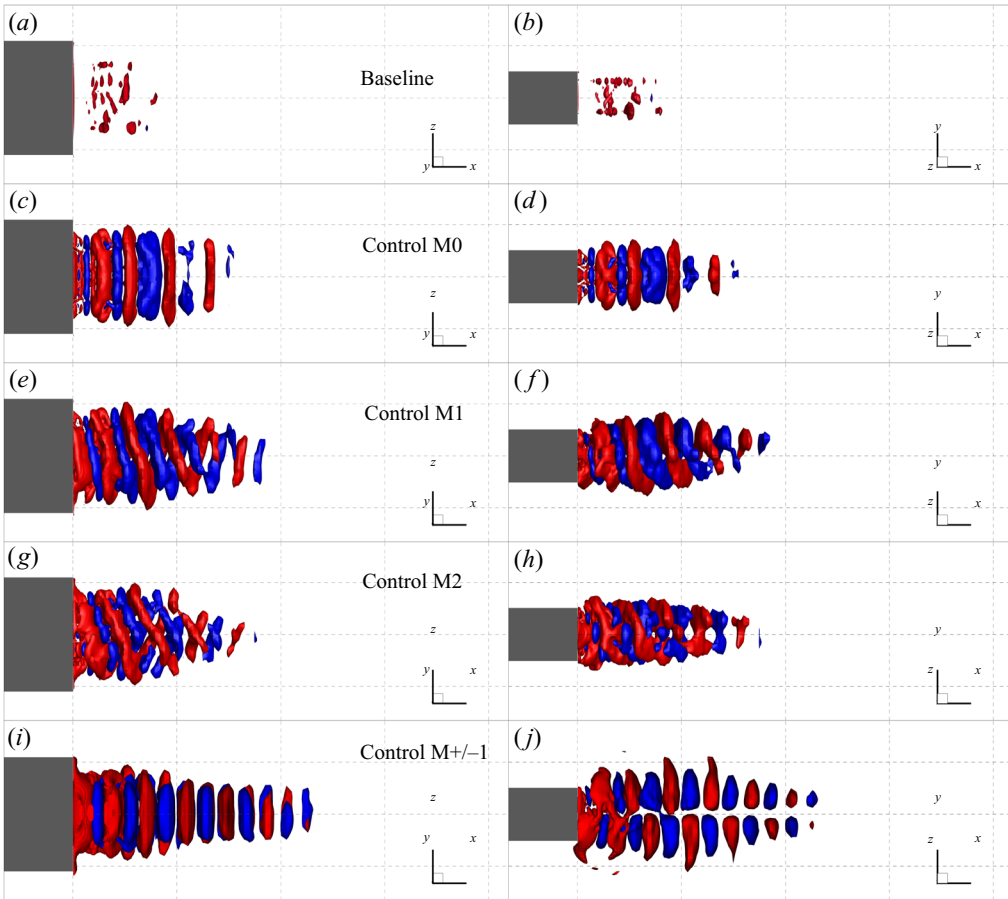


Figure 9. Instantaneous snapshot in the phase-averaged cycle of iso-levels of acoustic fluctuations at  $A_x = \pm 0.005$  for the baseline jet, projected onto the (a) major axis plane and (b) minor axis plane. Plots (c,d) show the corresponding results for the M0 forcing; (e,f) are corresponding results for the M1 forcing; (g,h) are corresponding results for the M2 forcing; (i,j) are corresponding results for the M+/-1 forcing. The distance between consecutive vertical and horizontal grid lines are  $2D_{eq}$  and  $1D_{eq}$ , respectively.

forcing, where the major axis plane has no significant response at the forcing frequency, due to the deactivated actuators on the shorter edges of the nozzle.

Azimuthal variations in the near-field acoustic response of the jets at the forcing frequency are best visualized on a streamwise plane, as shown in figure 11. Phase-averaged dilatation at  $t_f/T_f = 0.5$  is shown for M0, M1, M2 and M+/-1 controlled cases at  $x \sim 4.5$ , which encompasses the peak amplitudes in the downstream acoustic band (seen earlier in figure 10).

The M0 forcing results in mostly concentric rings of acoustic radiation dominated by the axisymmetric mode, due to the synchronous firing of all actuators (figure 11a). Towards the near-field, the waves emitted from the longer edges display slightly higher amplitudes, which can be associated to the larger number of actuators placed there. This acoustic response resembles the signature of two acoustic monopoles separated by a small distance (Russell 2013). The downstream acoustic imprint of M1 forcing is a spiral around the jet centreline, as seen in figure 11(b). This follows the phase lag in the vortex intrusion events generated from successive actuators, consistent with the spiral pattern seen earlier in the shear layer

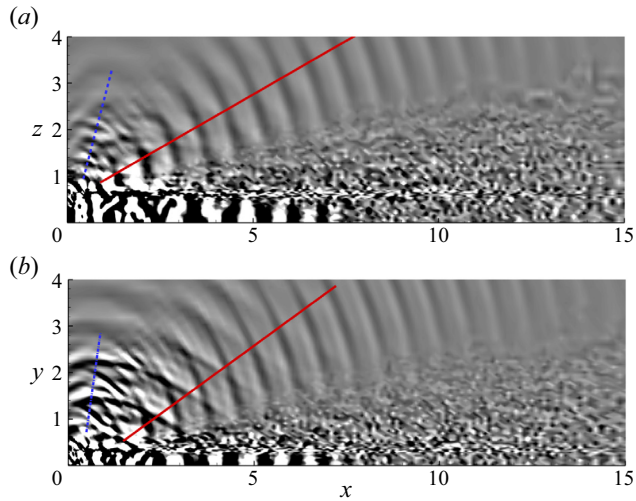


Figure 10. Instantaneous snapshot in the phase-averaged cycle of dilatation contours at a phase of  $\pi/2$  on the (a) major and (b) minor axis planes for the M0 forcing. Eleven contour levels are evenly distributed between  $-0.02$  and  $0.02$ .

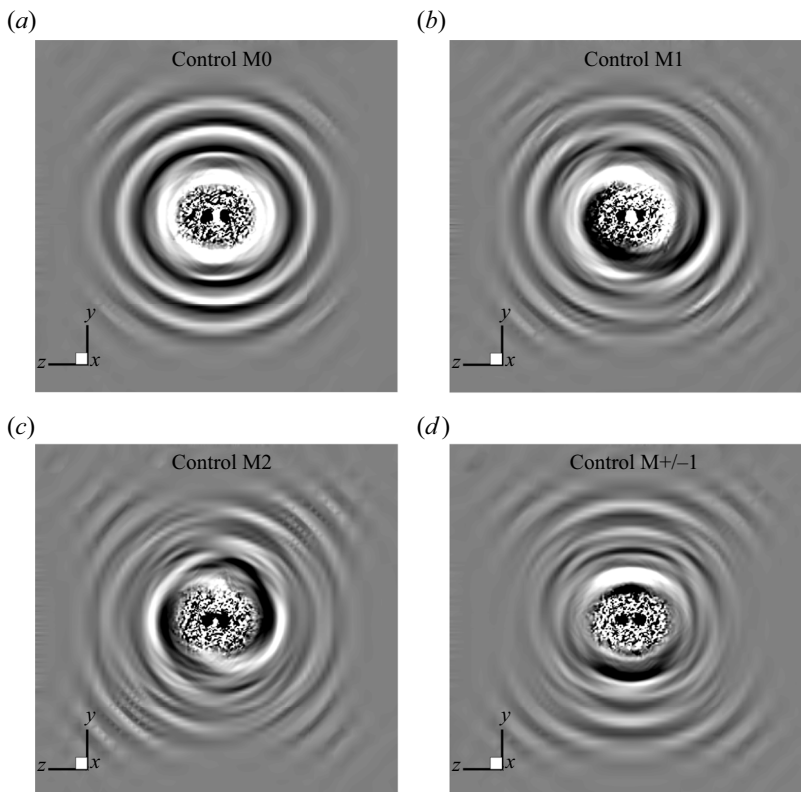


Figure 11. Instantaneous snapshot in the phase-averaged cycle of dilatation contours at a phase of  $\pi$  for the (a) M0, (b) M1, (c) M2 and (d) M+/-1 forcings. Eleven contour levels are evenly distributed between  $-0.01$  and  $0.01$ .

vortices in [figure 8](#). Compared with M0 forcing, M1 forcing results in relatively lower amplitudes of acoustic response in the near-field. The M2 forcing generates a double helix radiation pattern, shown in [figure 11\(c\)](#), that further weakens the near-field imprint of forcing. The M+/-1 forcing results in acoustic waves that are anti-symmetric about the  $z$  axis, as shown in [figure 11\(d\)](#). The out-of-phase action of the top and bottom set of actuators on the longer edges of the nozzle produces an acoustic dipole. Due to the destructive interference of these waves, the major axis plane experiences a reduction in the amplitude of forced acoustic response. These variations in the forced acoustic response of the jets have implications for far-field noise mitigation efforts, as will be later detailed in § 8.

## 7. Effect of actuation on radiative efficiency of the jet

The far-field sound signature of the jet is a consequence of its acoustic gain, that determines the energy content propagated outward from the plume. Since the component,  $\nabla \psi'_a$ , quantifies the acoustic fluctuations in the jet, the impact of various control strategies on noise mitigation can be discerned by studying its near-field properties. In this section we quantify various properties of the acoustic component in the baseline and controlled jets that are critical to determining the radiative efficiency of these jets. This is expected to provide a fundamental understanding of the efficacy of control, and reasoning for noise signature modification.

### 7.1. Convective speed

As previously identified in the literature, turbulent jets sustain large-scale coherent structures, in addition to fine-scale turbulence (Crow & Champagne 1971; Brown & Roshko 1974; Michalke & Fuchs 1975; Arndt, Long & Glauser 1997). In high-speed jets, supersonic convection of such coherent structures, which are often viewed as instability waves, leads to Mach wave radiation (Tam 1995; Nichols, Lele & Moin 2009), which significantly contributes to the acoustic signature of the jet. Therefore, here we evaluate the convective speed of acoustically relevant coherent structures using a wavenumber–frequency analysis.

[Figure 12](#) shows the spatio-temporal Fourier transform of the acoustic component,  $A_x$ , in the near-field. The data are obtained from a horizontal array of probes placed  $2.5D_{eq}$  away from the jet centreline, on the major axis plane. Data on the minor axis plane shows qualitatively similar trends, and are not included for brevity. The abscissa shows the streamwise wavenumber ( $k$ ), the ordinate shows frequency ( $St$ ) and the contour levels show the logarithm of energy. The streamwise wavenumber,  $k$ , is non-dimensionalized as  $k = k^*D_{eq}^*$ , where  $k^*$  is the dimensional wavenumber and  $D_{eq}^*$  is the nozzle equivalent diameter. Since the energy contribution from upstream propagating waves is substantially less than that from downstream propagating waves, only the positive wavenumbers are depicted in these contours. The convective speed is proportional to the slope,  $St/k$ , which is equivalent to  $(1/2\pi)\omega/k$ , where  $\omega$  is the non-dimensional circular frequency. Relevant phase speeds of the flow,  $U_j - c_j$ ,  $c_j$  and  $U_j + c_j$ , are shown using a blue dotted line, red dashed line and green dashed-dot line, respectively. Here,  $U_j$  is the jet exit velocity and  $c_j$  is the speed of sound based on jet exit conditions. Peak energy within this acoustic wavepacket propagates at a velocity of about  $0.7U_j$ , which is close to the jet exit sonic speed. Energy content that propagates at supersonic convective speeds and, thus, contributes to far-field acoustic emissions is located to the left of the red dashed line.

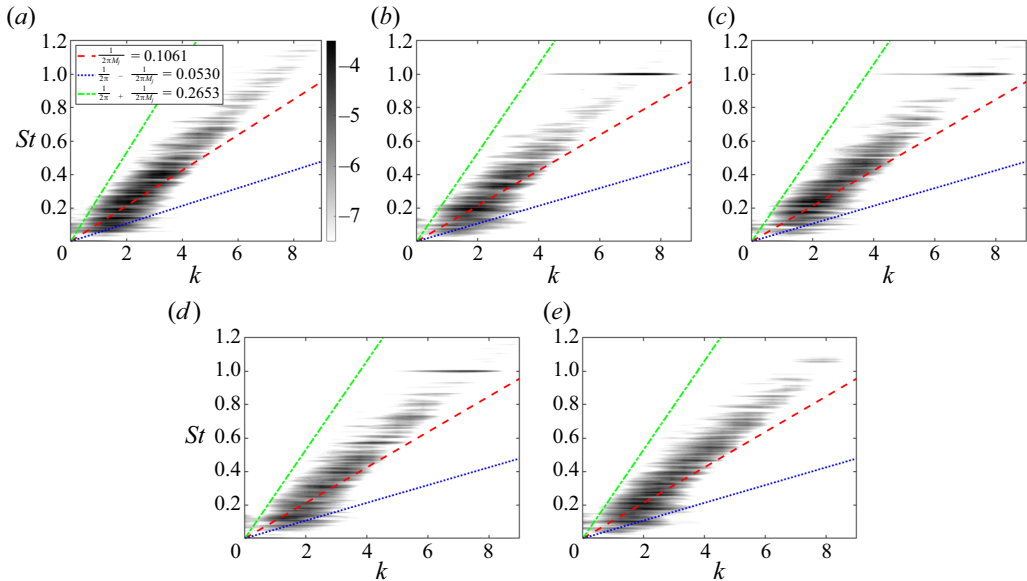


Figure 12. Wavenumber–frequency spectra of acoustic fluctuations on the major axis plane for the (a) baseline jet, (b) M0 forcing, (c) M1 forcing, (d) M2 forcing and (e) M+/-1 forcing.

The acoustic wavepacket has most of the energy in the radiation zone (since the convective hydrodynamic component has been removed from this field). The baseline jet (figure 12a) displays energy peaks within  $0.1 \leq St \leq 0.5$ , with minimal radiation below  $St \sim 0.1$ . Although higher frequencies radiate, their energy content is significantly lesser than that in the vicinity of the jet column mode. In the controlled jets, the shear layer actuation, in general, reduces the above-mentioned column-mode peaks in the supersonic regime. With M0 forcing (figure 12b), energy reduction within the supersonic radiating band is achieved primarily at column-mode frequencies below  $St \sim 0.4$ , and at higher frequencies within  $0.7 \leq St \leq 1$ , in the vicinity of the forcing frequency. Similar inferences can be drawn for M1 forcing (figure 12c), where column-mode energy reduction is observed in the frequencies surrounding  $St \sim 0.3$ . The M2 forcing (figure 12d) shows the most attenuation in column-mode energy among all the controlled simulations studied. The peak energy bands seen in the baseline case have been significantly reduced with M2 control. Energy reduction achieved in M+/-1 forcing (figure 12e) is comparable to that in M0 forcing, at frequencies below  $St \sim 0.4$ .

Along with the reduction of supersonic energy content, actuation results in the fundamental tone, seen as a peak in the controlled cases. While M+/-1 forcing does not display this peak in the major axis plane, it is observed in the near-field acoustic component on the minor axis plane. Among these actuation patterns, M2 forcing exhibits minimal tonal amplitudes. This along with the most reduction in supersonic column-mode energy makes M2 forcing efficient at mitigating noise emissions.

Below we further quantify the energy reduction in the supersonic radiating regime of column-mode frequencies. The energy distribution across various convective speeds is plotted at two frequencies,  $St = 0.3$  and  $St = 0.4$ , in figure 13. The abscissa displays the phase speed, and the ordinate is the logarithm of the power spectral density. Vertical lines identify significant phase speed values, corresponding to the slow acoustic wave (dotted line,  $U_j - c_j$ ), sonic speed at the jet exit (solid line,  $c_j$ ), jet exit velocity (dashed-dotted line,  $U_j$ ) and the fast acoustic wave (dashed line,  $U_j + c_j$ ). These plots are shown for both

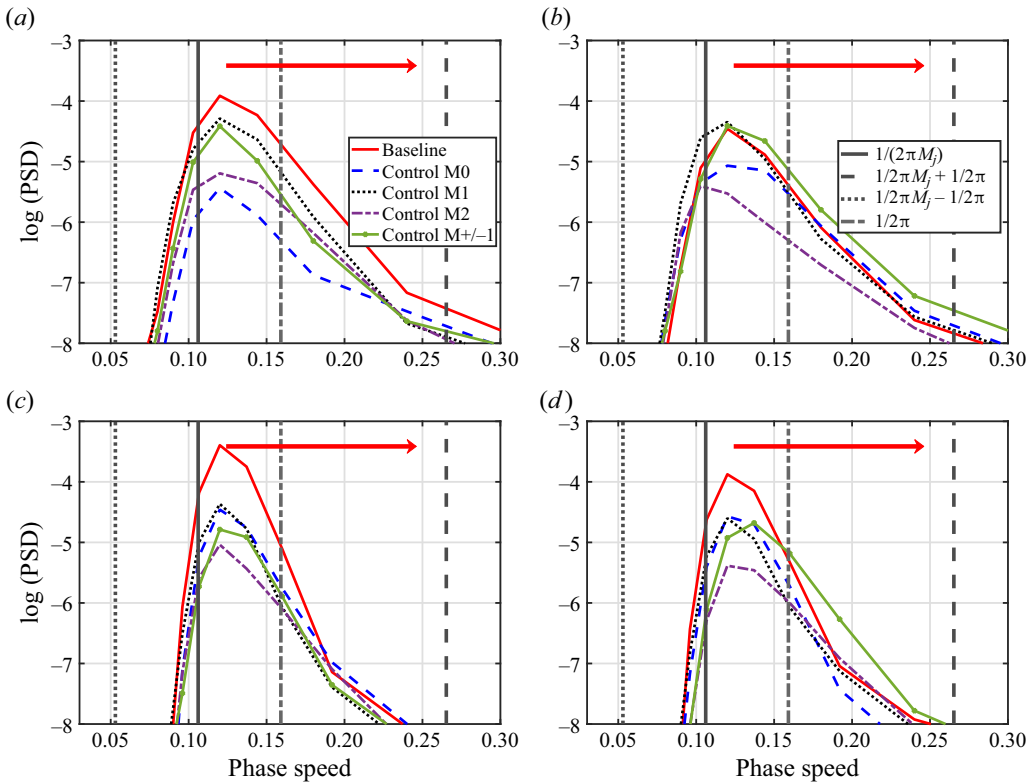


Figure 13. Distribution of the power spectral density with respect to phase speed at (a,b)  $St = 0.3$  and (c,d)  $St = 0.4$ . Left and right columns correspond to major and minor axis planes, respectively.

major (figure 13a,c) and minor axis planes (figure 13b,d). Energy content to the right of the solid black line has a supersonic convective wave speed and contributes to acoustic radiation, and is indicated by the red arrow.

Since the sampling location ( $2.5D_{eq}$  away from the jet centreline) is closer to the shear layer on the major axis plane than that on the minor axis plane (due to the AR of the jet), fluctuation amplitudes and absolute energy content is slightly higher on the major axis plane. In the baseline jet, peak energy content is present within the supersonic phase speed. With control, this energy peak reduces to varying levels in all cases. For all the controlled jets, the energy reduction is higher on the major axis plane than on the minor axis plane. At  $St = 0.3$ , the reduction levels are similar between the M1 and M+/-1 forcing on both planes. The M0 forcing shows the largest energy reduction at  $St = 0.3$  on the major axis plane, but M2 forcing is more consistent in achieving significant reductions in energy on both planes. At  $St = 0.4$ , M0, M1 and M+/-1 forcings show similar levels of energy reduction on both planes, while M2 forcing has the largest reduction on both planes. Thus, the effect of control is to reduce the energy content within the supersonic radiating regime, with M2 forcing being the most effective forcing strategy.

### 7.2. Coherence of acoustic wavepackets

Advection of coherent turbulent structures in the jet mixing layer results in large-scale oscillations, which can be interpreted as wavepackets with specific growth and decay

Number of snapshots	Sampling frequency (St)	Window	Overlap	Number of blocks ( $n_{blk}$ )	Number of frequencies ( $n_{ffi}$ )
2000	10	256	50 %	14	256

Table 3. Parameters used for spectral proper orthogonal decomposition.

rates (Jordan & Colonius 2013; Cavalieri, Jordan & Lesshafft 2019). They also behave as non-compact acoustic sources leading to noise characteristics with a distinct directivity (Sinha *et al.* 2014; Papamoschou 2018). The azimuthal coherence of these acoustic wavepackets have been shown to govern their radiating efficiency into the far field (Michalke & Fuchs 1975), with lower azimuthal modes being more efficient acoustic radiators. Thus, the impact of control on the spatio-temporal and azimuthal coherence of these wavepackets are studied via a 3-D spectral proper orthogonal decomposition (SPOD) (Towne, Schmidt & Colonius 2018; Schmidt & Colonius 2020) of the acoustic component. This is performed over a subdomain spanning  $0 \leq x \leq 15$ ,  $-2 \leq y \leq 2$  and  $-2 \leq z \leq 2$ . The parameters used for this decomposition are detailed in table 3.

The eigenvalue spectra for the leading two SPOD modes are shown in figures 14(a) and 14(b), respectively. For the baseline jet, a broadband peak exists between  $0.15 \leq St \leq 0.4$ , with peak eigenvalue magnitudes at  $St \sim 0.3$ , in both the leading modes. In the leading SPOD mode, control results in a broadband reduction of eigenvalue magnitudes within  $0.15 \leq St \leq 0.45$  in all cases, and induces peaks at the forcing frequency,  $St = 1$ , and its superharmonic,  $St = 2$ . The M2 forcing achieves most reduction in eigenvalues near the column-mode frequencies, consistent with the energy reduction seen in wavenumber–frequency spectra. The M0 and M2 forcings also show reduction above column-mode frequencies, between  $0.6 \leq St \leq 0.8$ . Peaks at the forcing frequency and the superharmonic are minimal in the M2 forcing, consistent with previous observations. In the second SPOD mode, the effects of control are relatively smaller. However, a broadband reduction is seen with M0 and M2 forcings, while M1 and M+/-1 forcings show similar eigenvalue magnitudes as in the baseline jet. Furthermore, the forcing tones are completely accounted for in the leading SPOD mode, with minimal representation in the higher modes.

The rank gap (defined as the difference between the leading two eigenvalues) provides a measure of the effectiveness of the control in redistributing energy across a broader range of spatio-temporal scales. Therefore, a smaller rank gap is a desirable quality to achieve noise source weakening. This is quantified in figure 14(c) for the baseline and controlled jets. A significant gap exists between the two dominant SPOD modes of the acoustic component in the baseline jet, indicating a low-rank behaviour, particularly near the column mode. Control reduces this rank gap, with peak reduction in M2 forcing, observed in the spectral range,  $0.15 \leq St \leq 0.4$ , which contributes to the peak noise radiation from this jet. This redistribution of energy into subdominant modes of the acoustic wavepacket reduces the probability of coherent structures resulting in large-scale radiation events.

To evaluate the spatial coherence in the acoustic wavepacket, we now present the SPOD modes and its azimuthal composition. It has to be noted that although the near-nozzle shear layer is non-axisymmetric due to the nozzle geometry, the near-field acoustic component of this AR = 2 : 1 jet lends itself to efficient representation using azimuthal Fourier modes, centred around the jet centreline (Chakrabarti *et al.* 2021). Key observations on its structure in the presence of control can be identified using a representative frequency,



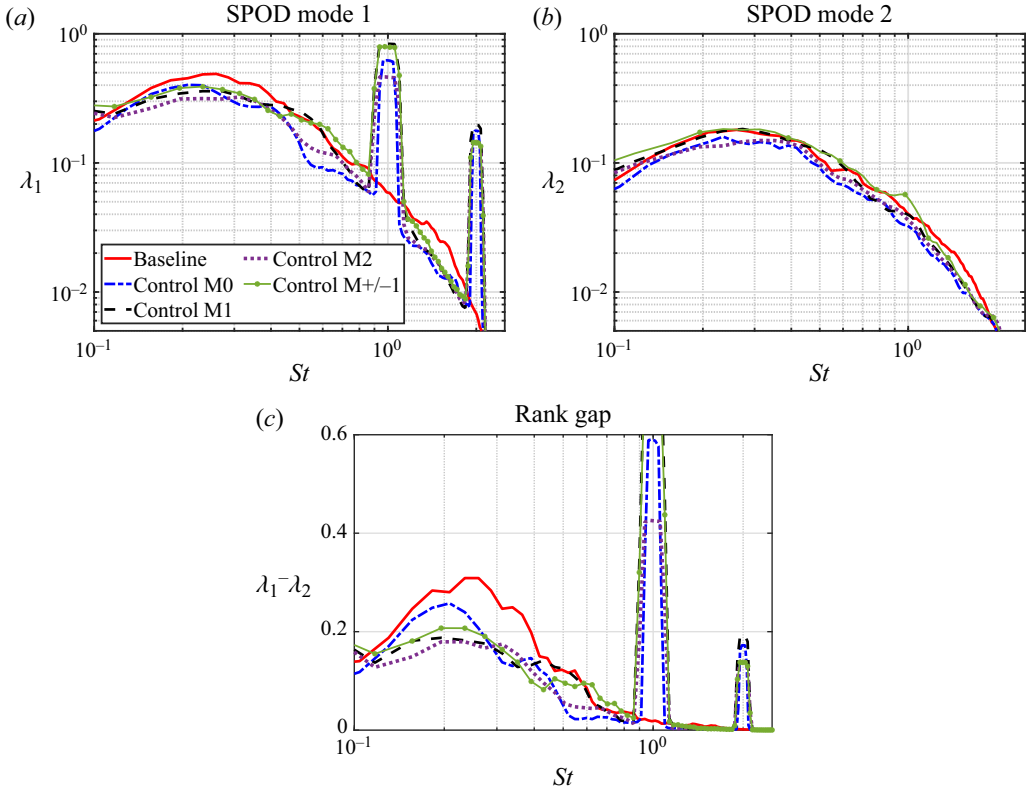


Figure 14. (a,b) Eigenvalue spectra comparison for the first two most energetic modes, respectively. (c) Rank gap between the first two dominant modes.

$St = 0.3$ . The acoustic wavepacket from the baseline case (figure 15a) is compared with that in M2 forcing (figure 15b) for brevity, since it shows the largest reduction in eigenvalue magnitudes near the column-mode frequencies. The azimuthal composition of each SPOD mode is identified using its Fourier decomposition, resulting in azimuthal modes. The first three azimuthal modes for each SPOD mode are included in the subsequent columns, to highlight key variations with control. The azimuthal decomposition is performed as

$$q(x, r, \phi) = q_a^0(x, r) + \sum_{m=1}^{\infty} [q_a^m(x, r) \cos(m\phi) + q_b^m(x, r) \sin(m\phi)], \quad (7.1)$$

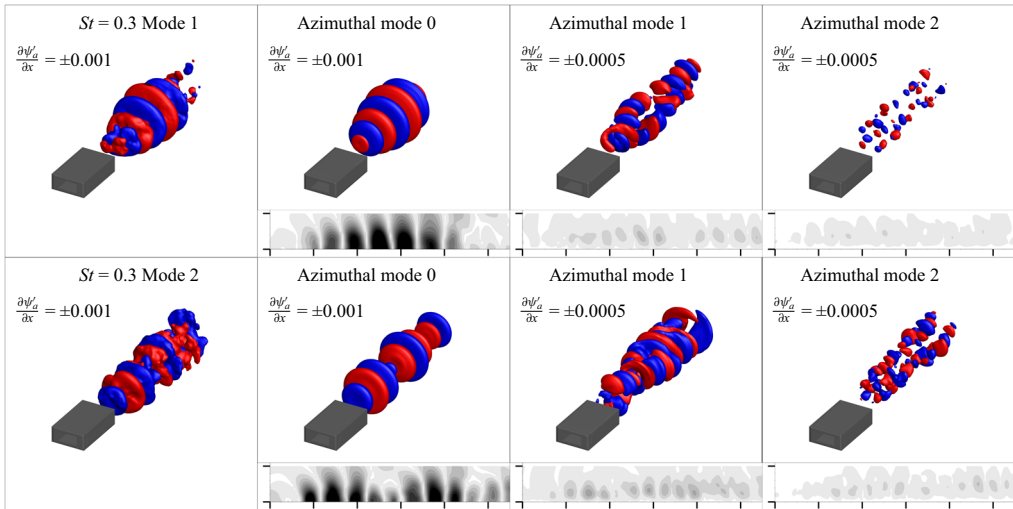
where  $m$  refers to the azimuthal mode number and  $q_a^m(x, r)$  and  $q_b^m(x, r)$  are the azimuthally invariant spatial supports determined by

$$q_a^0(x, r) = \frac{1}{2\pi} \int_{-\pi}^{\pi} q(x, r, \phi) \, d\phi, \quad (7.2)$$

$$q_a^m(x, r) = \frac{1}{\pi} \int_{-\pi}^{\pi} q(x, r, \phi) \cos(m\phi) \, d\phi, \quad (7.3)$$

$$q_b^m(x, r) = \frac{1}{\pi} \int_{-\pi}^{\pi} q(x, r, \phi) \sin(m\phi) \, d\phi. \quad (7.4)$$

(a)



(b)

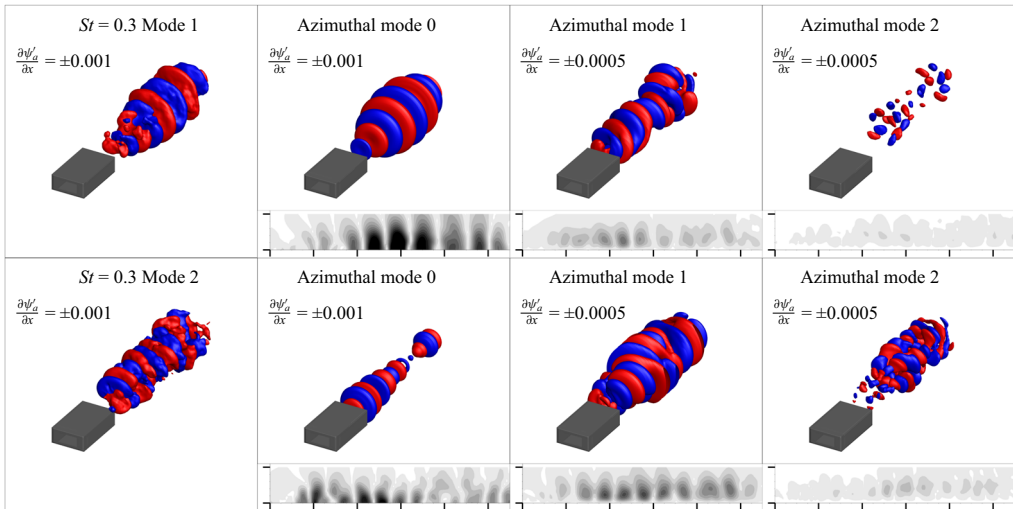


Figure 15. (a) Iso-levels of the leading two SPOD modes of acoustic fluctuations in the baseline jet at a frequency of  $St = 0.3$ , and its azimuthally decomposed Fourier modes. The first column shows the SPOD modes, while the subsequent columns show the corresponding three azimuthal Fourier modes. Plot (b) shows the same results for the M2 controlled jet. Inset figures below each azimuthal mode show contours of the corresponding spatial coefficients,  $\sqrt{q_a^2 + q_b^2}$ . Spatial extent of the contour plots is  $0 \leq x \leq 11$  and  $0 \leq r \leq 2$ . The ticks on the contour plot axes are spaced at  $2D_{eq}$ . Contour levels are uniformly distributed from 0.0001 to 0.005.

Azimuthal origin ( $\phi = 0$ ) is set at the minor axis plane of the jet (+ve y axis). For each azimuthal mode, suitable iso-levels are chosen to qualitatively describe its spatial extent. For quantitative comparisons, inset images with contours of  $\sqrt{(q_a^m)^2 + (q_b^m)^2}$  for each azimuthal mode are also shown. In the explanation that follows, the term ‘mode’ refers

to the SPOD mode (column 1), whereas ‘ $\phi$  mode’ refers to the azimuthal mode obtained through Fourier decomposition.

The coherent structures at  $St = 0.3$  in both the leading modes of the baseline have a dominantly axisymmetric nature. The spatially localized growth and decay of the acoustic wavepacket is consistent with findings on energetic structures by Arndt *et al.* (1997) and Colonius & Freund (2002) in circular jets, Chakrabarti *et al.* (2021); Lakshmi Narasimha Prasad & Unnikrishnan (2023a) in rectangular jets and Lakshmi Narasimha Prasad *et al.* (2022) in diamond jets. The axisymmetric  $\phi$ -mode 0 contains the majority of the energy due to the low AR of this jet. The spatial supports of  $\phi$ -mode 1 and  $\phi$ -mode 2 show a depreciating trend. The higher  $\phi$  modes are mostly confined to the corners of the nozzle.

The M2 forcing enhances the higher  $\phi$  modes of the acoustic wavepacket, as seen in figure 15(b). While mode 1 still retains a largely axisymmetric behaviour, its  $\phi$ -mode 1 shows significant amplification in relation to the baseline. This azimuthal redistribution of energy is more evident in mode 2, where the spatial support of  $\phi$ -mode 0 is severely attenuated, and confined towards the core of the jet near the centreline. Its  $\phi$ -mode 1 has a stronger spatial support as evidenced by the higher intensities in the spatial coefficients, visible in the corresponding inset contour. Its  $\phi$ -mode 2 also undergoes amplification, particularly away from the nozzle exit. Therefore, M2 forcing facilitates percolation of energy from  $\phi$ -mode 0 into  $\phi$ -mode 1 and 2. This modification to the dominant acoustic modes of the jet is beneficial (Michalke & Fuchs 1975), since lower/higher azimuthal modes have higher/lower downstream radiative efficiency. Thus, control not only redistributes energy into subdominant modes, it also redistributes energy into higher  $\phi$  modes, which is favourable for reducing noise radiation from the jet.

### 7.3. Nonlinear interactions

As seen in the preceding spectral analysis, the actuation results in redistribution of acoustic energy into the forcing frequencies and its harmonics. These phenomena occur through nonlinear interactions that manipulate spectral and azimuthal content in the acoustic wavepackets, which is the focus of this section.

To identify the azimuthal and spectral distribution of energy in the controlled jets, the acoustic component,  $A_x$ , is first subjected to an azimuthal decomposition, which extracts its  $\phi$  modes. Following this, SPOD is performed on each of the first ten  $\phi$  modes. The resulting eigenvalue spectra of the leading SPOD mode for the first six  $\phi$  modes are shown in figure 16. Results are presented for the M0 and M1 forcing, due to their unique response patterns. The abscissa shows frequency ( $St$ ) while the ordinate represents the  $\phi$  modes. The contour levels depict the logarithm of the eigenvalue magnitude obtained from the decomposition. In the following, the frequency-azimuthal response is represented using the ordered pair,  $(n_{St}, n_m)$ . Here,  $n_{St}$  is the ‘ $n$ th’ harmonic of the forcing (e.g.  $n_{St} = 1$  represents the forcing frequency);  $n_m$  represents the ‘ $n$ th’ azimuthal mode (e.g.  $n_m = 0$  corresponds to the axisymmetric  $\phi$  mode).

The M0 forcing (figure 16a) excites (1, 0) as expected, indicating that the wavepacket has a largely axisymmetric structure, consistent with the forcing wavepacket seen in § 6.2.1. Higher even  $\phi$  modes ((1, 2), (1, 4), etc.) are also excited due to the combined effects of the nozzle AR and corner vortices, but with progressively lower magnitudes. The superharmonic, (2, 0), and its higher even  $\phi$  modes are also excited with M0 forcing. The M2 forcing also results in a similar pattern, and is not included for brevity. The M1 forcing (figure 16b) generates odd  $\phi$  modes (1, 1), (1, 3), (1, 5), etc., at the fundamental

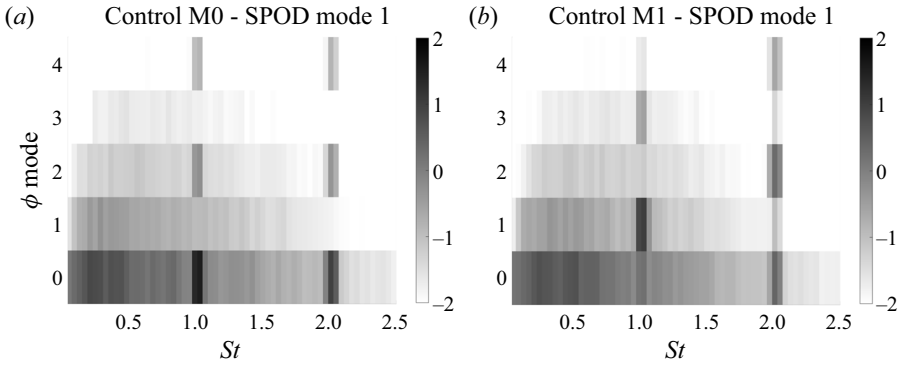


Figure 16. Eigenvalue spectra at various  $\phi$  modes for (a) M0 control and (b) M1 control.

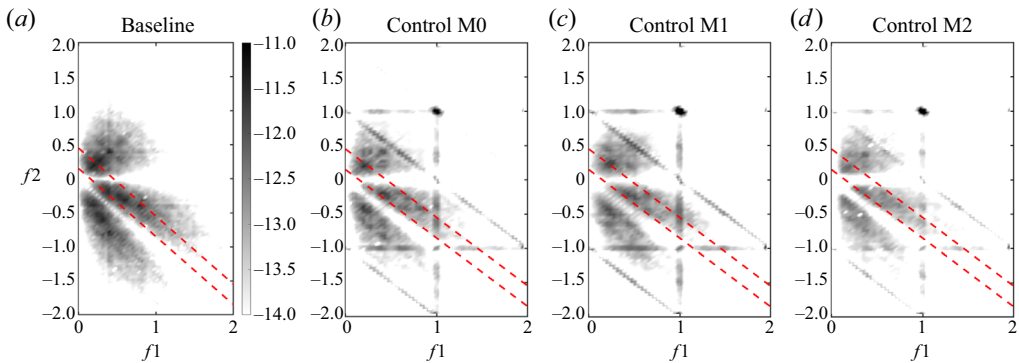


Figure 17. (Magnitude) mode bi-spectrum for the (a) baseline jet, (b) M0 forcing, (c) M1 forcing and (d) M2 forcing. The red dashed line corresponds to frequencies around the jet column mode.

forcing frequency. However, its superharmonic frequency exists at even  $\phi$  modes, (2, 0), (2, 2), (2, 4), etc.

Since the spectrum of the forcing signal does not contain energy at  $St = 2$ , as seen earlier in figure 3, the above superharmonic is a result of nonlinear interactions in the flow response. In the following, we characterize these nonlinear interactions in the jet plume, by evaluating dominant triadic interactions within the acoustic wavepacket, using bi-spectral analysis. The bi-spectrum identifies genesis of a new frequency/wavenumber resulting from nonlinear interactions of two other frequencies/wavenumbers (Kim *et al.* 1980; Nekkanti *et al.* 2023). The results are obtained using a bi-spectral mode decomposition as detailed in Schmidt (2020), on the 3-D field of the acoustic component,  $A_x$ .

The bi-spectrum for the baseline and M0, M1, M2 forcing cases are presented in figures 17(a), 17(b), 17(c) and 17(d), respectively. The abscissa and ordinate show a set of frequencies that nonlinearly interact and generate a third frequency, which is interpreted as the sum of the interacting frequency pair. The red dashed slanted lines demarcate all the pair of interactions that nonlinearly generate frequencies surrounding the jet column mode, between  $0.15 \leq St \leq 0.4$ , which are responsible for peak noise levels. The negative axis of frequencies represent difference interactions between the relevant pair.

The baseline case (figure 17a) has high magnitudes in the above-mentioned column-mode band, that nonlinearly energizes the dominant acoustic response of the jet. An interesting observation is that the column-mode band is mostly generated due to the

difference interactions of relatively higher frequencies. In comparison to the baseline case, nonlinear generation of the column-mode band is progressively reduced in the M0, M1 and M2 forcings, with the M2 forcing achieving the most reduction of almost one order of magnitude. The bi-spectrum of the controlled cases also confirms that the energy peak at  $St = 2$  is generated from the sum interaction of the forcing frequency (i.e.  $f_1 = 1, f_2 = 1, f_3 = f_1 + f_2 = 2$ ).

The following wave interaction is used to demonstrate that the superharmonic,  $St = 2$ , will mostly sustain even  $\phi$  modes irrespective of the azimuthal nature of forcing. Consider a wave with unit amplitude of the form

$$g(m, \omega) = \exp(i(m\phi - \omega t)), \quad (7.5)$$

where  $m$  is the positive or negative integer azimuthal mode number and  $\omega$  is the circular frequency. Using the relation,  $\omega = 2\pi f$ ,

$$g(m, f) = \exp(i(m\phi - 2\pi ft)), \quad (7.6)$$

where  $f$  is the non-dimensional frequency ( $St$ ). Nonlinear interaction of two such waves at frequencies,  $f_1$  and  $f_2$ , and azimuthal modes,  $m_1$  and  $m_2$ , can be represented as

$$\begin{aligned} g(m_1, f_1)g(m_2, f_2) &= \exp(i(m_1\phi - 2\pi f_1 t)) \exp(i(m_2\phi - 2\pi f_2 t)) \\ &= \exp(i(m_1 + m_2)\phi) \exp(-i2\pi(f_1 + f_2)t). \end{aligned} \quad (7.7)$$

Considering a resultant frequency,  $f_1 + f_2 = 2$ , as in the bi-spectrum above,

$$g(m_3, 2) = \exp(i(m_3\phi - 4\pi t)), \quad (7.8)$$

where  $m_3 = m_1 + m_2$ . For M0 forcing, the  $\phi$  modes dominant at the forcing frequency are  $m = 0, \pm 2, \pm 4$ , etc. Therefore, their mutual interactions,  $m_3 = m_1 + m_2$ , are either zero or are even integers, as observed in [figure 16\(a\)](#). The M1 forcing results in  $\phi$  modes,  $m = \pm 1, \pm 3, \pm 4$ , etc. Again, any combination of these modes always yields either a zero or an even integer, causing the superharmonic frequency to possess an even  $\phi$  mode structure.

These observations highlight the fact that there are significant spatio-temporal nonlinearities that energize the column-mode frequencies. Localized arc filament plasma actuator based control can subdue those triadic interactions responsible for peak noise radiation, and can nonlinearly modify the azimuthal structure of the acoustic wavepacket.

#### 7.4. Intermittency

Intermittent events resulting in bursts of acoustic energy contribute significantly to the peak far-field noise levels of the jet (Crawley & Samimy 2014). To identify the effect of control on acoustically relevant intermittency, we utilize a Morse wavelet (Lilly & Olhede 2009, 2012) transform on the near-field acoustic component. Data are sampled on the major and minor axis planes at  $\theta \sim 32^\circ$ ,  $2.5D_{eq}$  away from the jet centreline. Results are shown in [figure 18](#), using contours of the wavelet coefficient magnitude. The red solid line demarcates the cone of influence that separates the accurate region (within the cone) from the erroneous zone (outside the cone), resulting from wavelets that extend past the boundaries of the observation interval. Since frequencies  $0.15 \leq St \leq 0.4$  are the most energetic and contribute to peak noise levels, events occurring in this band are of interest and are shown by the red dashed lines in the contours.

The acoustic component in the baseline jet contains several energetic intermittent events on both the major and minor axis planes (within the frequency band of interest), which

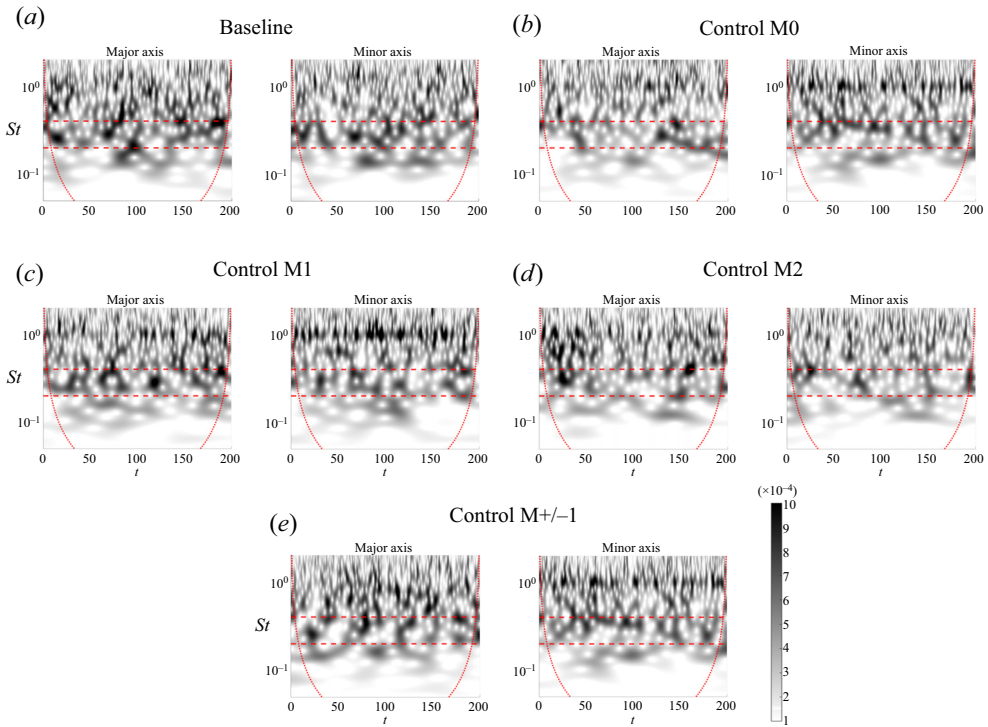


Figure 18. Scalograms of the acoustic fluctuations at  $r = 2.5$ ,  $\theta \sim 32^\circ$ , on the major axis and minor axis planes. Solid red curves demarcate the cone of influence, while the horizontal dashed red lines highlight the frequency band of interest.

directly contribute to far-field sound (Unnikrishnan & Gaitonde 2016). Control reduces these intermittent events, with the degree of reduction depended on the forcing strategy. The M0 and M1 forcing shows intermittency reduction on both planes, with M0 being relatively more effective. The M2 forcing is the most successful in reducing intermittent acoustic events, with the best performance achieved on the minor axis plane, in terms of minimizing the amplitude and number of occurrences of intermittent events. In M+/-1 forcing, intermittency reduction is evident on the minor axis plane, but not on the major axis plane, due to the forcing pattern. Furthermore, all the controlled jets display increased intermittency at the forcing frequency, resulting from the downstream acoustic band, shown earlier in figure 10.

In order to better quantify intermittency effects, histograms are plotted in figure 19. The ordinate corresponds to the ratio of the number of occurrences in a specific bin to the overall number of occurrences, and the abscissa denotes the scalogram magnitude. Thus, the plots represent the probability of occurrence of these time-frequency localized events between the frequency bands of interest ( $0.15 \leq St \leq 0.4$ ) shown in figure 18. The brown solid line demarcates a threshold chosen to identify an energetic intermittent event in this frequency band. This representative threshold of  $7 \times 10^{-4}$  is close to the upper limit of the contour levels shown in figure 18. Thus, bins to the right of this threshold identify strong intermittent events that are of interest.

The baseline histogram in figure 19 shows high probability of energetic intermittent events, which are reduced upon forcing the jet. For example, compared with the baseline case, M2 forcing has a cumulative reduction of  $\sim 65\%$  and  $\sim 55\%$  on the major and minor

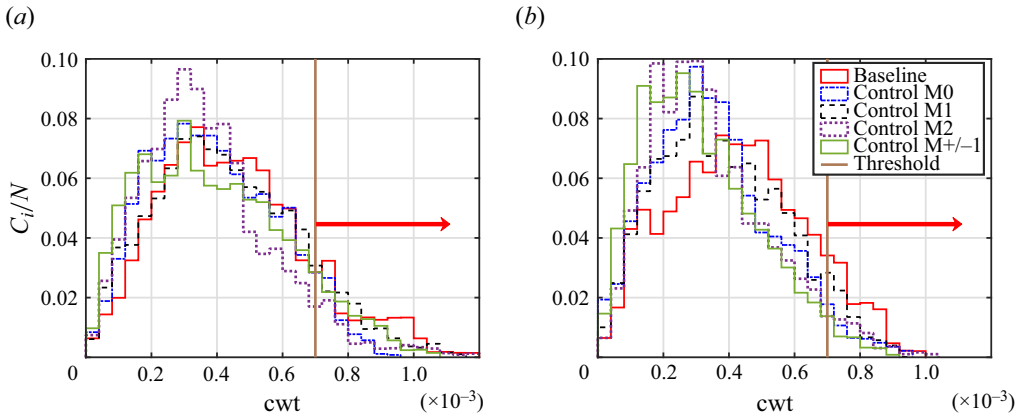


Figure 19. Histograms depicting probability of occurrence of time-frequency localized events between  $0.15 \leq St \leq 0.4$  at various scalogram magnitudes on the (a) major axis plane and (b) minor axis plane. The solid brown line represents the threshold of the scalogram magnitude chosen to quantify a significant event. The red arrow denotes the region of interest.

axis planes, respectively. Other controlled cases also follow similar trends, as identified in the preceding discussion on scalograms. Along with the reduction in high-amplitude events, the histograms also show a shift in peak probability to lower wavelet coefficient magnitudes. This indicates that, even if these intermittent events were to occur within the jet, the energy content, and hence, their far-field noise signature will be much lower. This shift is quantified through the skewness values of the histograms, that highlight the asymmetry in the distribution. The baseline jet has a skewness of 0.269 and  $-0.196$  on the major and minor axis planes, respectively. A negative skewness indicates that the mode of the distribution is located to the right of its mean (i.e. higher wavelet coefficient magnitude), and has a long tail towards the left of the distribution (i.e. lower wavelet coefficient magnitude). With the imposition of M2 control for example, the skewness increases to 0.717 on the major axis plane and 0.590 on the minor axis plane. This indicates that the mode has shifted to the left of the mean (i.e. lower wavelet coefficient magnitude) with a long narrow tail to the right. The steeper probability roll off in controlled cases at high scalogram magnitudes demonstrates that the likelihood of intermittent events that produce sound waves at peak energy-containing frequencies has decreased.

Thus, the foregoing analyses has identified that, by (a) reducing energy in the supersonic regime at peak radiating frequencies and redistributing it into an energy band at the forcing frequency, (b) exciting higher azimuthal modes and smaller spatial scales, (c) reducing the energization of column-mode frequencies by limiting nonlinear triadic interactions, and (d) reducing extreme intermittent events within the jet that are responsible for bursts of acoustic energy, the control (in particular, M2 forcing) is successful in achieving a flow response conducive to noise mitigation.

## 8. Far-field acoustics

Having established the advantageous manner in which the control manipulates the turbulence and acoustic response within the plume, we now summarize the far-field impact of actuation, which ultimately determines the utility of the present approach as a noise control strategy. To this end, we compare the far-field noise levels in the baseline and controlled jets, along a polar arc at a radial distance,  $r = 40D_{eq}$ , from the nozzle exit.

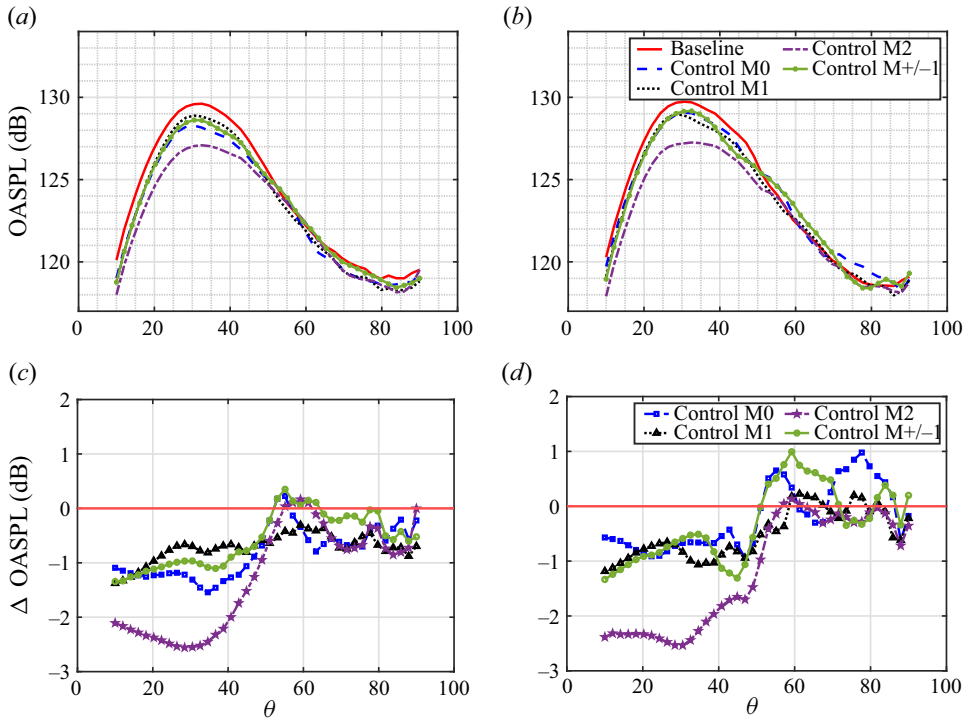


Figure 20. Far-field OASPL comparison between the uncontrolled jet and jets with control at various polar angles on the (a) major axis and (b) minor axis planes. Corresponding OASPL differences between controlled jets and the baseline jet on the (c) major axis and (d) minor axis planes. Red horizontal lines in panels (c,d) indicate the 0 dB datum.

The OASPL variation with polar angle,  $\theta$  (as measured from the jet downstream direction), for the baseline and the controlled cases are shown in figure 20(a,b), on the major axis and minor axis planes, respectively. The corresponding change in OASPL from the baseline jet,  $\Delta$ OASPL, is also included in figure 20(c,d), for better quantification. Here  $\Delta$ OASPL is defined as

$$\Delta\text{OASPL} = \text{OASPL}_{\text{Controlled}} - \text{OASPL}_{\text{Baseline}}. \quad (8.1)$$

The 0 dB datum is indicated by the horizontal red line. Noise amplification/reduction with implementation of control are represented by positive/negative  $\Delta$ OASPL values.

Peak noise levels exist at shallow downstream angles,  $25^\circ \leq \theta \leq 45^\circ$ , as seen in figure 20(a,b). Noise levels are significantly lower (by  $\sim 10$  dB) along sideline angles,  $70^\circ \leq \theta \leq 90^\circ$ , compared with peak noise levels. The baseline jet displays similar OASPL on the major and minor axis planes, which is in line with the symmetric far-field acoustics seen for rectangular jets with low ARs operating at perfectly expanded conditions (Bridges 2012; Heeb *et al.* 2013; Chakrabarti *et al.* 2021). The OASPL are reduced in all controlled cases, both at peak radiating angles and at very-low polar angles. The reduction achieved along downstream angles,  $10^\circ \leq \theta \leq 50^\circ$ , is higher than that along jet sideline angles,  $70^\circ \leq \theta \leq 90^\circ$ . The M2 forcing results in the best noise mitigation among these cases on both the major and minor axis planes, with most reduction in OASPL occurring at angles  $10^\circ \leq \theta \leq 50^\circ$ .

The  $\Delta$ OASPL plots (figure 20c,d) further clarify the above trends. With M0 forcing, a peak noise reduction of  $\sim 1.5$  dB is attained on the major axis plane, while a consistent



$\sim 1$  dB decrease is observed at angles of peak noise radiation on the minor axis plane. The M0 forcing also increases noise levels by  $\sim 0.8$  dB at  $\theta \sim 80^\circ$ , which can be attributed to strong actuation tones (as shown earlier in § 7.1). This is particularly true of the minor axis plane, due to the placement of more actuators along the longer edge of the nozzle. Peak noise reduction for M1 forcing is  $\sim 0.75$  dB on the major axis plane and  $\sim 1$  dB on the minor axis plane. However, relative to M0 forcing, M1 forcing is effective at reducing the forcing tones, thus reducing the sideline noise on both principal planes. Peak noise reduction for M+/-1 forcing is  $\sim 1$  dB on the major axis plane and  $\sim 0.75$  dB on the minor axis plane. Similar to the M0 forcing, M+/-1 forcing also results in strong tones, which almost completely eliminates noise mitigation for  $\theta > 50^\circ$ . Even though the actuators on the shorter edges of the nozzle are deactivated for M+/-1 forcing, noise reduction is seen on the major axis plane, resulting from the coupled dynamics of the shear layers on the two planes.

Consistent with the near-field analysis of § 7, peak noise levels exhibit the greatest reduction with M2 forcing on both planes, as seen in figure 20(c,d). Noise reduction of  $> 2$  dB is consistently observed on both planes at angles,  $20^\circ \leq \theta \leq 40^\circ$ , with a peak reduction of  $\sim 2.6$  dB at  $\theta \sim 34^\circ$ . It demonstrates the efficacy of this control in attenuating dominant sound sources of this jet, since this polar angle coincides with the angle where the baseline jet exhibits the highest OASPL. Noise levels along the sideline polar angles are either comparable to or lesser than those of the other controlled jets. The generally larger noise reduction seen on the major axis plane can be attributed to the better reduction in energy content within the supersonic radiating regime seen in § 7.1. It is observed that the reduction in peak noise levels saturate at a phase difference of  $\pi/2$  between adjacent actuators, with comparable results for M2, M3 and  $M\pi$  forcings. For brevity, these results have been summarized in Appendix A.

The spectral bands that contribute to the above identified noise mitigation are evaluated using the far-field sound pressure level (SPL) spectra. Figure 21(a,b) plots the SPL spectra at  $\theta = 34^\circ$ , which is the polar angle of peak noise levels on the major and minor axis planes, respectively. Figure 21(c,d) are the corresponding spectra along a representative sideline angle,  $\theta = 80^\circ$ . The downstream spectra (figure 21a,b) of the baseline jet contain a broadband peak at  $0.2 \leq St \leq 0.4$  with steep roll off at higher frequencies. The M0 forcing results in noise reduction within this broadband hump and its approximate superharmonic range,  $0.6 \leq St \leq 0.8$ , which is most evident on the major axis plane, consistent with the  $\Delta$ OASPL plots discussed earlier. A strong tone at the forcing frequency ( $St = 1$ ) is also evident. Although the far-field spectra of M1 forcing are comparable to those of M0 forcing, the SPL reduction at the peak energy-containing frequencies is less than that in M0 control on the major axis plane. This also explains why M1 control in figure 20(c) showed a smaller reduction in OASPL. The spectra for M+/-1 forcing have limited reduction in energy contained within the column-mode broadband hump on both planes. The peak reduction seen for M2 forcing results from significantly lower energy at  $0.1 \leq St \leq 0.45$ , combined with its comparatively lower forcing tones. Along the jet sideline (figure 21c,d), all the controlled cases exhibit reduced SPL on the major axis plane for  $0.4 \leq St \leq 0.8$ . The key difference is the strong tones in M0 forcing (on both the planes) and M1 forcing (on the minor axis plane).

Among the cases evaluated, M2 azimuthal forcing produces the most desirable acoustic impact through column-mode mitigation and minimal imprint of the actuation tone. Additionally, it induces only minor modifications to the mean flow characteristics, while attenuating the dominant noise mechanisms in the jet. The current forcing strategies are informed by a simplified linear analysis and practical considerations in the

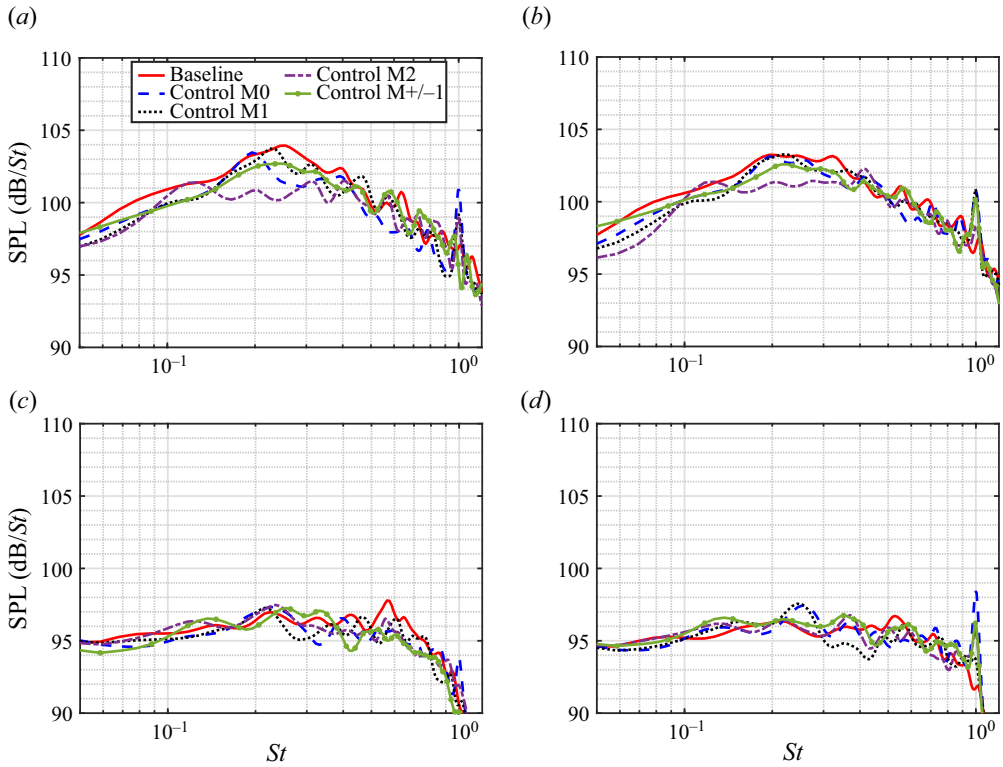


Figure 21. The SPL comparison of results from the baseline jet and jets with control at a peak noise radiating angle of  $\theta = 34^\circ$ , on the (a) major axis and (b) minor axis. Plots (c,d) show the corresponding results at a jet sideline angle of  $\theta = 80^\circ$ .

corresponding experimental configuration. However, the physical insights obtained into the response of rectangular shear layers and their acoustic components to LAFPA-based actuators can be leveraged by future efforts to further the noise reduction capabilities of small-perturbation-based control strategies. In addition, a multi-dimensional linear analysis of non-homogeneous basic states associated with these rectangular jets could further refine the spatial and temporal forcing parameters, to improve the control authority of the actuators.

### 9. Conclusion

We utilize a high-fidelity simulation approach to evaluate the effects of LAFPA-based control on coherent structures and acoustic emissions from rectangular shear layers. A 2 : 1 AR Mach 1.5 rectangular jet is subjected to control with the objective of manipulating the evolution of coherent shear layer structures in a manner conducive to far-field noise reduction. The design of LAFPA actuators, which includes eight actuators around the periphery of the nozzle, and their duty cycle are decided based on prior experimental and computational inferences.

A preliminary linear analysis using NS-MFP is performed to characterize the receptivity of the baseline time-averaged flow to shear layer actuation. Based on the NS-MFP linear spectrum, the highest cumulative amplification is achieved within the shear layer at a frequency of  $St = 1$  ( $St_\theta = 0.0068$ ). Therefore, in the nonlinear simulations the shear layer

is forced at  $St = 1$ , at experimentally informed sequences, including M0, M1, M2, M3 and  $M\pi$ , that progressively increase the phase difference between successive actuators, and  $M+/-1$ , which corresponds to the flapping mode of the jet.

In general, all controlled simulations show only minor variations in the mean flow features. The M0 forcing that induces the strongest vortical shear layer response displays a slightly lower centreline velocity decay, spreading rate, and consequentially, a longer potential core. The M1 and  $M+/-1$  forcings show similar trends albeit to a smaller extent, and M2, M3 and  $M\pi$  forcings result in a mean flow almost identical to the baseline jet. The TKE along the jet lip line is significantly reduced until the core collapse location in all cases, which is attributed to decreased production and increased convection.

The vortical and acoustic responses to actuation in the turbulent plume identify critical flow features that tailor the far-field noise signature of the jets. The vortical response includes a set of spanwise vortices when the actuators turn on and a set of streamwise-elongated lambda vortices when the actuators turn off. In M0 forcing the streamwise nature is dominant, and the synchronized firing results in a circumferentially coherent vortex ring. Due to the phase difference between actuators, M1 forcing produces circumferentially slanted structures with an enhanced 3-D nature. The M2 forcing effectively combines the above two features, producing streamwise elongated vortical elements with circumferential variability. The response to  $M+/-1$  forcing is similar to M0, except for an out-of-phase nature between the two longer edges of the nozzle. The acoustic wavepacket excited as a response to actuation has an axially compact ( $x \leq 3Deq$ ) structure conforming to nozzle shape, with M0, M1, M2 and M3 forcings energizing the azimuthally invariant, single helix, double helix and triple helix structures, respectively. The acoustic response at the forcing frequency is dominated by a nonlinearly generated downstream band, and a relatively weaker sideline band resulting from the direct signature of the actuator.

These responses result in key near-field modifications to varying degrees (with M2 being the most effective), conducive to far-field noise reduction as summarized below. A wavenumber–frequency analysis reveals that control reduces energy contained at peak frequencies with supersonic phase speeds. As seen in the SPOD of the acoustic mode, energy is redistributed into sub-dominant modes, weakening the low-rank nature of the acoustic response. A study of the spatial structure of the acoustic wavepacket at the jet column-mode frequency identifies that control promotes activation of higher azimuthal modes, which are inefficient radiators of noise in comparison to the axisymmetric mode. In addition, energy transfer through (difference) triadic interactions in the plume that contribute to percolation of energy towards peak radiating frequencies are significantly reduced with the application of control, resulting in fewer sound-generating intermittent events.

In the far field the above flow modifications translate into lower noise levels. Peak noise levels decrease by approximately 1 dB to 1.5 dB for M0, M1 and  $M+/-1$  forcings on the major axis plane, and about 1 dB on the minor axis plane. The M2 forcing shows the maximum noise reduction of  $\sim 2.6$  dB on both planes, along the peak radiation direction of the jet. Noise levels in the sideline shows a modest decrease on the major axis plane, while M0,  $M+/-1$ , M3 and  $M\pi$  forcings slightly increase noise levels over the baseline. At polar angles corresponding to peak noise levels, far-field noise reduction is contributed by a reduction in the energy contained around the column-mode broadband hump. The effectiveness of M2 forcing accrued from the higher attenuation near column-mode frequencies and minimal amplitudes of the actuation tone. This benefit saturated beyond a

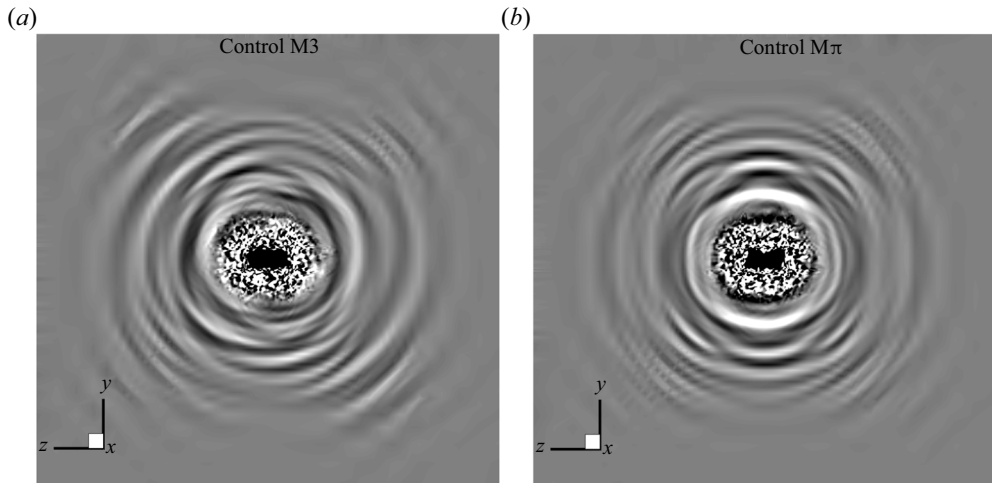



Figure 22. Instantaneous snapshot in the phase-averaged cycle of dilatation contours at a phase of  $\pi$  for the M3 and  $M\pi$  forcings. Eleven contour levels are evenly distributed between  $-0.01$  and  $0.01$ .

phase difference of  $\pi/2$  between adjacent actuators, yielding comparable results for M2, M3 and  $M\pi$  actuations. On the minor axis plane a stronger actuation tone for M0 and  $M+/-1$  forcings primarily contributes to the noise increase.

**Funding.** This research was supported by the Office of Naval Research, through grant no. N00014-21-1-2318, monitored by S. Martens.

**Declaration of interests.** The authors report no conflict of interest.

**Author ORCIDs.**

 Anirudh Lakshmi Narasimha Prasad <https://orcid.org/0000-0001-7802-2208>.

## Appendix A

As mentioned in § 3, the first- and second-order statistics, as well as far-field acoustic benefits, were relatively invariant for the controlled cases when the phase difference between adjacent actuators was higher than  $\pi/2$ . Therefore, M2, M3 and  $M\pi$  cases generated mostly comparable performances. A few differences observed in their acoustic responses are now summarized here for completeness, by comparing these cases with the baseline.

### A.1. Acoustic directivity

Azimuthal variations in the near-field acoustic response of the jets controlled with M3 and  $M\pi$  forcings along a streamwise plane at  $x \sim 4.5$  is shown in figure 22. As expected, M3 forcing generates a downstream-directed band at the forcing frequency ( $St = 1$ ), in the form of a triple helix. The  $M\pi$  forcing has a stronger tonal response on the minor axis plane. Consistent with the trends discussed in figure 11, the near-field amplitude of the forcing tone reduces with increasing phase difference between adjacent actuators.

## Noise mitigation in rectangular jets

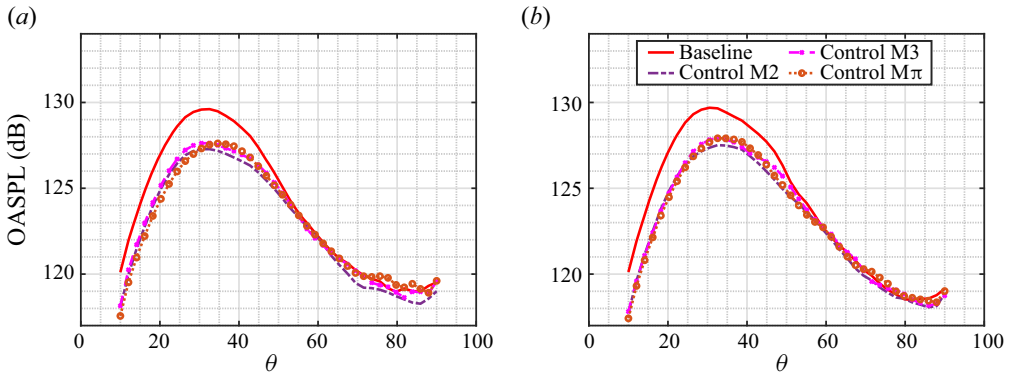


Figure 23. The OASPL differences between controlled jets and the baseline jet on the (a) major axis and (b) minor axis planes. Red horizontal lines indicate the 0 dB datum.

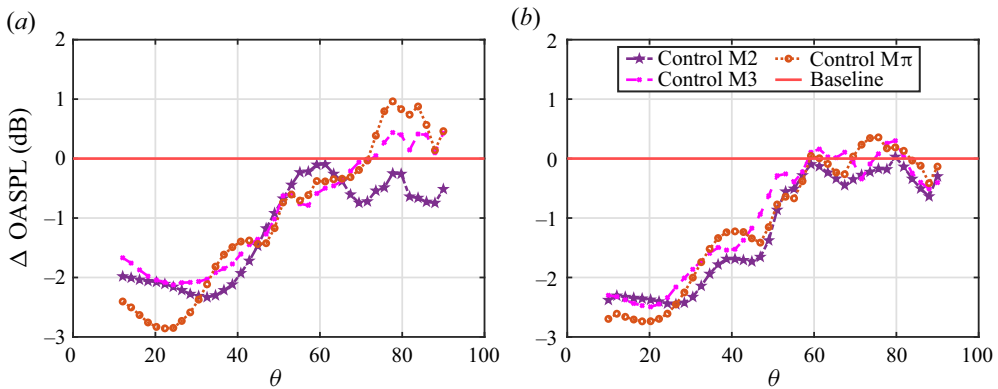


Figure 24. The OASPL differences between controlled jets and the baseline jet on the (a) major axis and (b) minor axis planes. Red horizontal lines indicate the 0 dB datum.

### A.2. Far-field acoustics

Since M2, M3 and  $M\pi$  produced comparable far-field benefits, these three cases are presented along with the baseline in [figure 23](#), to highlight some subtle differences. Overall sound pressure levels comparison between the baseline and controlled jets are presented in [figure 23\(a,b\)](#) on the major and minor axis planes, respectively. The corresponding change in OASPL with respect to that of the baseline jet is shown in [figure 24\(a,b\)](#), respectively. Generally, M2, M3 and  $M\pi$  yield similar levels of peak noise reduction, with the following distinctions. Along the peak radiating angle ( $\theta \sim 34^\circ$ ), M2 achieves the most noise reduction, with its benefit more evident on the minor axis plane. At very-low polar angles ( $\theta \leq 25^\circ$ ) where the OASPLs are at least 3 dB lesser than the peak noise level,  $M\pi$  forcing results in a quieter jet. However, M3 and  $M\pi$  actuations result in increased noise levels along the sideline direction ( $\theta \geq 65^\circ$ ), especially on the major axis plane.

The above far-field acoustic trends indicate that for low-AR perfectly expanded jets, increasing the phase difference between adjacent actuators beyond  $\pi/2$  (M2 forcing) has minimal impact on the acoustic benefit obtained at polar angles seeing peak noise levels.

At this forcing configuration, the mean flow and acoustic response are seen to reach a saturation point for the actuator configuration tested.

REFERENCES

- ADLER, M.C., GONZALEZ, D.R., STACK, C.M. & GAITONDE, D.V. 2018 Synthetic generation of equilibrium boundary layer turbulence from modeled statistics. *Comput. Fluids* **165**, 127–143.
- ALVI, F.S., LOU, H., SHIH, C. & KUMAR, R. 2008 Experimental study of physical mechanisms in the control of supersonic impinging jets using microjets. *J. Fluid Mech.* **613**, 55–83.
- ARNDT, R.E.A., LONG, D.F. & GLAUSER, M.N. 1997 The proper orthogonal decomposition of pressure fluctuations surrounding a turbulent jet. *J. Fluid Mech.* **340**, 1–33.
- BHAUMIK, S., GAITONDE, D.V., UNNIKRISHNAN, S., SINHA, A. & SHEN, H. 2018 Verification and application of a mean flow perturbation method for jet noise. *Aerosp. Sci. Technol.* **80**, 520–540.
- BIRCH, S., LYUBIMOV, D., BUCHSHTAB, P., SECUNDOV, A. & YAKUBOVSKY, K. 2005 Jet-pylon interaction effects. In *11th AIAA/CEAS Aeroacoustics Conference*, p. 3082.
- BLAZEK, J. 2001 Computational fluid dynamics: principles and applications. In *Boundary Conditions*, 1st edn, p. 270. Elsevier Science.
- BOGEY, C. 2022 Interactions between upstream-propagating guided jet waves and shear-layer instability waves near the nozzle of subsonic and nearly ideally expanded supersonic free jets with laminar boundary layers. *J. Fluid Mech.* **949**, A41.
- BOGEY, C. & BAILLY, C. 2010 Influence of nozzle-exit boundary-layer conditions on the flow and acoustic fields of initially laminar jets. *J. Fluid Mech.* **663**, 507–538.
- BRÈS, G.A., YEUNG, B., SCHMIDT, O.T., GHASSEMI ISFAHANI, A., WEBB, N.J., SAMIMY, M. & COLONIUS, T. 2021 Towards large-eddy simulations of supersonic jets from twin rectangular nozzle with plasma actuation. In *AIAA AVIATION 2021 Forum*, p. 2154.
- BRIDGES, J. 2012 Acoustic measurements of rectangular nozzles with bevel. In *18th AIAA/CEAS Aeroacoustics Conference (33rd AIAA Aeroacoustics Conference)*, p. 2252.
- BROWN, C. 2008 Scalability of the localized arc filament plasma actuators. In *14th AIAA/CEAS Aeroacoustics Conference (29th AIAA Aeroacoustics Conference)*, p. 3043.
- BROWN, G.L. & ROSHKO, A. 1974 On density effects and large structure in turbulent mixing layers. *J. Fluid Mech.* **64** (4), 775–816.
- CAVALIERI, A.V.G., JORDAN, P. & LESSHAFFT, L. 2019 Wave-packet models for jet dynamics and sound radiation. *Appl. Mech. Rev.* **71** (2), 020802.
- CHAKRABARTI, S., GAITONDE, D.V. & UNNIKRISHNAN, S. 2021 Representing rectangular jet dynamics through azimuthal fourier modes. *Phys. Rev. Fluids* **6** (7), 074605.
- CLARKSON, B.L. 1959 The effect of jet noise on aircraft structures. *Aeronaut. Q.* **10** (2), 103–126.
- COLONIUS, T. & FREUND, J. 2002 Pod analysis of sound generation by a turbulent jet. In *40th AIAA Aerospace Sciences Meeting & Exhibit*, p. 72.
- COLONIUS, T., LELE, S.K. & MOIN, P. 1997 Sound generation in a mixing layer. *J. Fluid Mech.* **330**, 375–409.
- CRAWLEY, M. & SAMIMY, M. 2014 Decomposition of the near-field pressure in an excited subsonic jet. In *20th AIAA/CEAS Aeroacoustics Conference*, p. 2342.
- CROW, S.C.J. & CHAMPAGNE, F.H. 1971 Orderly structure in jet turbulence. *J. Fluid Mech.* **48** (3), 547–591.
- DOAK, P.E. 1989 Momentum potential theory of energy flux carried by momentum fluctuations. *J. Sound Vib.* **131** (1), 67–90.
- GAITONDE, D.V. 2012 Analysis of the near field in a plasma-actuator-controlled supersonic jet. *J. Propul. Power* **28** (2), 281–292.
- GAITONDE, D.V. & SAMIMY, M. 2010 Effect of plasma-based azimuthal mode excitation on supersonic jet flow. In *5th Flow Control Conference*, p. 4416.
- GAITONDE, D.V. & SAMIMY, M. 2011 Coherent structures in plasma-actuator controlled supersonic jets: axisymmetric and mixed azimuthal modes. *Phys. Fluids* **23** (9), 095104.
- GARMANN, D.J. 2013 Characterization of the vortex formation and evolution about a revolving wing using high-fidelity simulation. PhD thesis, University of Cincinnati.
- GEORGIADIS, N. & PAPAMOSCHOU, D. 2003 Computational investigations of high-speed dual stream jets. In *9th AIAA/CEAS Aeroacoustics Conference and Exhibit*, p. 3311.
- GHASSEMI ISFAHANI, A., WEBB, N.J. & SAMIMY, M. 2021a Control of coupling in twin rectangular supersonic jets. In *AIAA AVIATION 2021 Forum*, p. 2122.
- GHASSEMI ISFAHANI, A., WEBB, N.J. & SAMIMY, M. 2021b Coupling modes in supersonic twin rectangular jets. In *AIAA Scitech 2021 Forum*, p. 1292.

- GHASSEMI ISFAHANI, A., WEBB, N.J. & SAMIMY, M. 2022 Effects of active control on flow and near-and far-field acoustics of twin rectangular supersonic jets. In *AIAA SCITECH 2022 Forum*, p. 2401.
- GOJON, R., GUTMARK, E.J. & MIHAESCU, M. 2019 Antisymmetric oscillation modes in rectangular screeching jets. *AIAA J.* **57** (8), 3422–3441.
- GONZÁLEZ, D.R., GAITONDE, D.V. & LEWIS, M.J. 2015 Large-eddy simulations of plasma-based asymmetric control of supersonic round jets. *Intl J. Comput. Fluid Dyn.* **29** (3–5), 240–256.
- GRINSTEIN, F.F. 1995 Self-induced vortex ring dynamics in subsonic rectangular jets. *Phys. Fluids* **7** (10), 2519–2521.
- GUTMARK, E. & HO, C.-M. 1983 Preferred modes and the spreading rates of jets. *Phys. Fluids* **26** (10), 2932–2938.
- GUTMARK, E.J. & GRINSTEIN, F.F. 1999 Flow control with noncircular jets. *Annu. Rev. Fluid Mech.* **31** (1), 239–272.
- GUTMARK, E.J., SCHADOW, K.C. & BICKER, C.J. 1990 Near acoustic field and shock structure of rectangular supersonic jets. *AIAA J.* **28** (7), 1163–1170.
- HEEB, N.S., MORA SANCHEZ, P., GUTMARK, E.J. & KAILASANATH, K. 2013 Investigation of the noise from a rectangular supersonic jet. In *19th AIAA/CEAS Aeroacoustics Conference*, p. 2239.
- HELFER, T.M. 2011 Noise-induced hearing injuries, active component, us armed forces, 2007–2010. *Med. Surv. Mon. Rep.* **18** (6), 7–10.
- HUET, M., FAYARD, B., RAHIER, G. & VUILLOT, F. 2009 Numerical investigation of the micro-jets efficiency for jet noise reduction. In *15th AIAA/CEAS Aeroacoustics Conference (30th AIAA Aeroacoustics Conference)*, p. 3127.
- HUSSAIN, A.K.M.F. 1986 Coherent structures and turbulence. *J. Fluid Mech.* **173**, 303–356.
- ISFAHANI, A.G., WEBB, N.J. & SAMIMY, M. 2021 Control of flow and acoustics in twin rectangular jets. *AIAA Paper* 1292-2021.
- JORDAN, P. & COLONIUS, T. 2013 Wave packets and turbulent jet noise. *Annu. Rev. Fluid Mech.* **45**, 173–195.
- KHOBRADE, N., UNNIKRISHNAN, S. & KUMAR, R. 2022 Flow instabilities and impact of ramp–isolator junction on shock–boundary-layer interactions in a supersonic intake. *J. Fluid Mech.* **953**, A30.
- KIM, Y.C., BEALL, J.M., POWERS, E.J. & MIKSAD, R.W. 1980 Bispectrum and nonlinear wave coupling. *Phys. Fluids* **23** (2), 258–263.
- LAKSHMI NARASIMHA PRASAD, A., SALEH, Y., SELLAPPAN, P., UNNIKRISHNAN, S. & ALVI, F.S. 2022 Effects of expansion ratio and nozzle asymmetry on flowfield of diamond jets. *AIAA J.* **60** (9), 5215–5231.
- LAKSHMI NARASIMHA PRASAD, A. & UNNIKRISHNAN, S. 2023a Effect of LAFPA based control on supersonic rectangular jets. In *AIAA SCITECH 2023 Forum*, p. 1346.
- LAKSHMI NARASIMHA PRASAD, A. & UNNIKRISHNAN, S. 2023b Effect of plasma actuator-based control on flow-field and acoustics of supersonic rectangular jets. *J. Fluid Mech.* **964**, A11.
- LAKSHMI NARASIMHA PRASAD, A. & UNNIKRISHNAN, S. 2023c Flow-field and acoustics of azimuthally forced rectangular jets. In *AIAA AVIATION 2023 Forum*, p. 4178.
- LEAHY, R.P., GHASSEMI ISFAHANI, A., WEBB, N.J. & SAMIMY, M. 2022 The effects of active control on near-field pressure fluctuations in supersonic rectangular twin jets. In *28th AIAA/CEAS Aeroacoustics 2022 Conference*, p. 2968.
- LILLY, J.M. & OLHEDE, S.C. 2009 Higher-order properties of analytic wavelets. *IEEE Trans. Signal Process.* **57** (1), 146–160.
- LILLY, J.M. & OLHEDE, S.C. 2012 Generalized morse wavelets as a superfamily of analytic wavelets. *IEEE Trans. Signal Process.* **60** (11), 6036–6041.
- LIU, J., KHINE, Y.Y., SALEEM, M., LOPEZ RODRIGUEZ, O. & GUTMARK, E.J. 2022 Effect of axial location of micro vortex generators on supersonic jet noise reduction. In *AIAA SCITECH 2022 Forum*, p. 1791.
- LIU, X.-D., OSHER, S. & CHAN, T. 1994 Weighted essentially non-oscillatory schemes. *J. Comput. Phys.* **115** (1), 200–212.
- MARTENS, S. 2002 Jet noise reduction technology development at GE Aircraft Engines. *ICAS Paper* **842**.
- MICHALKE, A. 1965 On spatially growing disturbances in an inviscid shear layer. *J. Fluid Mech.* **23** (3), 521–544.
- MICHALKE, A. & FUCHS, H.V. 1975 On turbulence and noise of an axisymmetric shear flow. *J. Fluid Mech.* **70** (1), 179–205.
- NEKKANTI, A., SCHMIDT, O.T., MAIA, I., JORDAN, P., HEIDT, L. & COLONIUS, T. 2023 Bispectral mode decomposition of axisymmetrically and non-axisymmetrically forced turbulent jets. In *AIAA AVIATION 2023 Forum*, p. 3651.
- NICHOLS, J.W., LELE, S. & MOIN, P. 2009 Global mode decomposition of supersonic jet noise. In *Center for Turbulence Research Annual Research Briefs, Stanford, CA*.
- PAPAMOSCHOU, D. 2018 Wavepacket modeling of the jet noise source. *Intl J. Aeroacoust.* **17** (1–2), 52–69.

- PAPAMOSCHOU, D. & ROSHKO, A. 1988 The compressible turbulent shear layer: an experimental study. *J. Fluid Mech.* **197**, 453–477.
- PETERSEN, R.A. & SAMET, M.M. 1988 On the preferred mode of jet instability. *J. Fluid Mech.* **194**, 153–173.
- POINSOT, T.J. & LELE, S.K. 1992 Boundary conditions for direct simulations of compressible viscous flows. *J. Comput. Phys.* **101** (1), 104–129.
- PRASAD, C. & GAITONDE, D.V. 2022 A time-domain linear method for jet noise prediction and control trend analysis. *Aerosp. Sci. Technol.* **121**, 107377.
- PRASAD, C. & MORRIS, P.J. 2020 A study of noise reduction mechanisms of jets with fluid inserts. *J. Sound Vib.* **476**, 115331.
- PRASAD, C. & MORRIS, P.J. 2021 Steady active control of noise radiation from highly heated supersonic jets. *J. Acoust. Soc. Am.* **149** (2), 1306–1317.
- RANJAN, R., UNNIKRISHNAN, S. & GAITONDE, D.V. 2020 A robust approach for stability analysis of complex flows using high-order Navier–Stokes solvers. *J. Comput. Phys.* **403**, 109076.
- RANJAN, R., UNNIKRISHNAN, S., ROBINET, J.-C. & GAITONDE, D.V. 2021 Global transition dynamics of flow in a lid-driven cubical cavity. *Theor. Comput. Fluid Dyn.* **35**, 397–418.
- ROE, P.L. 1981 Approximate riemann solvers, parameter vectors and difference schemes. *J. Comput. Phys.* **43**, 357–372.
- ROSA, V. 2018 Rans-based prediction of noise from isothermal and hot subsonic jets. PhD thesis, University of Southampton.
- RUSSELL, D. 2013 Acoustics and vibration animations. Available at: <https://www.acs.psu.edu/drussell/demos.html>.
- SAMIMY, M., KIM, J.-H., KASTNER, J., ADAMOVICH, I. & UTKIN, Y. 2007a Active control of a Mach 0.9 jet for noise mitigation using plasma actuators. *AIAA J.* **45** (4), 890–901.
- SAMIMY, M., KIM, J.-H., KASTNER, J., ADAMOVICH, I. & UTKIN, Y. 2007b Active control of high-speed and high-Reynolds-number jets using plasma actuators. *J. Fluid Mech.* **578**, 305–330.
- SAMIMY, M., KIM, J.-H. & KEARNEY-FISCHER, M. 2009 Active control of noise in supersonic jets using plasma actuators. In *Turbo Expo: Power for Land, Sea, and Air*, vol. 48821, pp. 97–107.
- SAMIMY, M., KIM, J.-H., KEARNEY-FISCHER, M. & ADAMOVICH, I.V. 2008 Noise mitigation in supersonic jets using plasma actuators. *Tech. Rep.* RTO-MP-AVT-158. NATO.
- SAMIMY, M., KIM, J.-H., KEARNEY-FISCHER, M. & SINHA, A. 2010 Acoustic and flow fields of an excited high Reynolds number axisymmetric supersonic jet. *J. Fluid Mech.* **656**, 507–529.
- SAMIMY, M., WEBB, N., ESFAHANI, A. & LEAHY, R. 2023 Perturbation-based active flow control in overexpanded to underexpanded supersonic rectangular twin jets. *J. Fluid Mech.* **959**, A13.
- SCHMIDT, O.T. 2020 Bispectral mode decomposition of nonlinear flows. *Nonlinear Dyn.* **102** (4), 2479–2501.
- SCHMIDT, O.T. & COLONIUS, T. 2020 Guide to spectral proper orthogonal decomposition. *AIAA J.* **58** (3), 1023–1033.
- SHANNON, G., MCKENNA, M.F., ANGELONI, L.M., CROOKS, K.R., FRISTRUP, K.M., BROWN, E., WARNER, K.A., NELSON, M.D., WHITE, C. & BRIGGS, J. 2016 A synthesis of two decades of research documenting the effects of noise on wildlife. *Biol. Rev.* **91** (4), 982–1005.
- SHU, C.W. & OSHER, S. 1988 Efficient implementation of essentially non-oscillatory shock-capturing schemes. *J. Comput. Phys.* **77** (2), 439–471.
- SINHA, A., RODRÍGUEZ, D., BRÈS, G.A. & COLONIUS, T. 2014 Wavepacket models for supersonic jet noise. *J. Fluid Mech.* **742**, 71–95.
- SNYDER, R. 2007 Mixing control in supersonic rectangular jets using plasma actuators. PhD thesis, The Ohio State University.
- SPETH, R.L. & GAITONDE, D.V. 2013 Parametric study of a Mach 1.3 cold jet excited by the flapping mode using plasma actuators. *Comput. Fluids* **84**, 16–34.
- STEPHENS, D.G. & MAYES, W.H. 1979 Aircraft noise-induced building vibrations. In *Community Noise*. ASTM International.
- SUN, Y., TAIRA, K., CATTAFESTA, L.N. & UKEILEY, L.S. 2017 Spanwise effects on instabilities of compressible flow over a long rectangular cavity. *Theor. Comput. Fluid Dyn.* **31** (5), 555–565.
- TAM, C.K.W. 1995 Supersonic jet noise. *Annu. Rev. Fluid Mech.* **27** (1), 17–43.
- TOWNE, A., SCHMIDT, O.T. & COLONIUS, T. 2018 Spectral proper orthogonal decomposition and its relationship to dynamic mode decomposition and resolvent analysis. *J. Fluid Mech.* **847**, 821–867.
- UNNIKRISHNAN, S. & GAITONDE, D.V. 2016 Acoustic, hydrodynamic and thermal modes in a supersonic cold jet. *J. Fluid Mech.* **800**, 387–432.
- VALENTICH, G., UPADHYAY, P. & KUMAR, R. 2016 Mixing characteristics of a moderate aspect ratio screeching supersonic rectangular jet. *Exp. Fluids* **57** (5), 1–14.



## *Noise mitigation in rectangular jets*

- WEBB, N.J., GHASSEMI ISFAHANI, A., LEAHY, R. & SAMIMY, M. 2022 Active control of rectangular supersonic twin jets using perturbations: Effects and mechanism. In *AIAA SCITECH 2022 Forum*, p. 2401.
- WIEGAND, C. 2018 F-35 air vehicle technology overview. In *2018 Aviation Technology, Integration, and Operations Conference*, p. 3368.
- YEUNG, B. & SCHMIDT, O.T. 2023 Plasma actuation and bispectral mode decomposition of supersonic twin-rectangular jet flow. In *AIAA AVIATION 2023 Forum*, p. 4177.
- ZAMAN, K.B.M.Q. 1996 Axis switching and spreading of an asymmetric jet: the role of coherent structure dynamics. *J. Fluid Mech.* **316**, 1–27.